Master's Thesis

Numerical Investigation of First Stage Base Heat Flux of Secondary Nozzles in Bleed Engine and Gas Generator Cycles

prepared by

Yannik Feldner

from Hann. Münden

at the Institute of Aerodynamics and Flow Technology

Thesis Period:	1st June 2023 until 7th September 2023
Supervisor:	Dr. Moritz Ertl
First Referee:	Prof. Dr. rer. nat. Dr. habil. Andreas Dillmann
Second Referee:	Prof. Dr. Martin Rein

Abstract

The correct estimation and prediction of thermal loads acting on a launch vehicle plays a vital role in characterizing the requirements on the thermal protection system (TPS) of the spacecraft in order to avoid catastrophic failure. With the increasing demand for reusable launch vehicles (RLVs), which represent a resource- and cost-efficient alternative to conventional space transport systems, additional challenges in the assessment of the thermal loads arise due to the changing flow field during the return phase of the vehicle and especially the retro-propulsion and landing phase. While the flight trajectory and conditions are the same for RLVs and conventional space transport systems until MECO and stage separation, the counterflowing supersonic exhaust jets during the retro-burn have a strong effect on the thermal loads on the rocket structures and dominate the flowfield characteristics during this flight phase. While some studies on the base heating have been conducted for conventional launch vehicles [28] and RLVs [23], [44], [11], no published research has been devoted to the topic of side-effects due to the outflow of gas generators, bleed nozzles and air vents of cryogenic fuel tanks for both kinds of vehicles. Due to these secondary exhaust jets, unburned hydrogen, which is used to power the oxidizer and fuel pumps for the main combustion chamber, is ejected near the high temperature outflow of the main engines.

In order to fill this knowledge gap and provide an assessment of the additional influence on the thermal loads acting on the vehicle baseplate due to these secondary nozzles, steady state CFD simulations were carried out for a first stage without aerodynamic control surfaces and landing legs. For all simulations the second-order finite-volume DLR TAU code [34] was applied using the Reynolds-Averaged Navier-Stokes (RANS) equations together with a one-equation Spalart-Allmaras turbulence model. A reduced Jachmimowski mechanism is applied for the chemistry modelling in order to capture the potenital effects of post-combustion. A detailed description of the numerical setup is given, including the free stream conditions for the simulated trajectory points during the ascent and retro-burn phase, the geometrical configuration of the bleed nozzle arrangement and aft-bay design, as well as the procedure for local refinement methods. A main aspect of the numerical setup was the derivation of the secondary nozzle outflow. For the simulation of these secondary nozzles, two main engine cycles, represented by an expander bleed engine cycle and a gas generator cycle, were identified as suitable modelling options, since they represent two state-of the art restartable engine cycles. The functionality of these engine cycles was described and the procedure for deriving and rescaling the secondary nozzle chamber conditions from already existing configurations to match the chosen engine characteristics is discussed in detail. The chamber conditions are then used to conduct separate 2D axisymmetric nozzle simulations, to reproduce the outflow conditions of the secondary nozzles and interpolate them on the 3D mesh used in the flowfield simulations. Additionally a grid convergence study was conducted to confirm the validity of the numerical mesh and provide an estimate on the numerical

uncertainties.

The influence of the additional bleed nozzle outflow is analyzed by comparing simulations for the ascent and retro-burn phase with activated and deactivated bleed nozzles. For the case of activated bleed nozzles a significant change in flowfield and thermal loads can be observed. Despite the fact, that the massflow of the secondary nozzles makes up only about 2% of the main engine mass flow, the recirculation and entrainment of hot main engine exhaust observed in the case of deactivated secondary nozzles is prevented, leading to a shielding effect of the baseplate and a reduction of thermal loads. While the mean heat flux along the baseplate for the case of deactivated secondary nozzles is given by 48.2 kW/m^2 and 20.9 kW/m^2 for the ascent and retro-burn phase, these values are reduced to -18.9 kW/m^2 and -2.8 kW/m^2 for the configuration with activated bleed nozzles. The wall temperature in these simulations equals 600 K.

The influence of the applied main engine cycle was investigated, which only had a small influence on the base heat flux.

Representative points along the ascent and descent trajectory were investigated and the observed flow patterns were described. For the ascent phase a converging behaviour of the base heat flux can be seen until the distribution of the thermal loads along the baseplate becomes independent of the increasing ambient pressure. During the retro-propulsion phase only three of the main engines are active, leading to a shielding effect against the incoming free stream. In case of activated bleed nozzles the observed heat flux values are in the negative range, indicating a reduction of the thermal loads compared to simulations with deactivated secondary nozzles.

The presented results clarify the necessity of including the outflow from secondary nozzles in heat flux predictions of launcher configurations, both for conventional space transport systems and RLVs, to provide accurate assessments of the aerothermal loads on the vehicle base.

Keywords: Reusable launch vehicle, retro-propulsion, bleed nozzle, thermal loads, aerothermal, RANS, supersonic exhaust jet, gas generator, baseplate, chemical modelling, post-combustion, CFD, flowfield analysis, first stage, base heating

Contents

Contents

List of Figures

List of Tables

Nomenclature

Latin letters

Variable	Definition	Unit
A_e	nozzle exit area	m^2
A_t	nozzle throat area	m^2
c	speed of sound	$\frac{m}{s}$
c_0	speed of sound in an undisturbed medium	$\frac{m}{s}$
c_p	specific heat capacity for constant pressure	$\frac{\mathrm{J}}{\mathrm{K}}$
c_v	specific heat capacity for constant volume	$\frac{\mathrm{J}}{\mathrm{K}}$
D_{main}	exit diameter of the main engines	m
D_{SN}	exit diameter of the secondary nozzles	m
e	internal energy	$\frac{\mathrm{kg\ m}^2}{\mathrm{s}^2}$
E_a	activation energy	$\frac{\mathrm{kg\ m}^2}{\mathrm{s}^2}$
e_a^{21}	relative error between the medium and fine grid flow variable	$-$
e_a^{32}	relative error between the coarse and medium grid flow variable	$-$
e_{ext}^{21}	relative extrapolated error for the fine-grid convergence index	$-$
e_{ext}^{32}	relative extrapolated error for the fine-grid convergence index	$-$
$e_{\mathrm{fine/medium}}$	relative error of the integrated heat flux between the fine and medium mesh	$-$
$e_{\mathrm{med/coarse}}$	relative error of the integrated heat flux between the medium and coarse mesh	$-$
$\mathrm{GCI}_{\mathrm{fine}}^{21}$	fine-grid convergence index	$-$

Nomenclature

Variable	Definition	Unit
$\text{GCI}^{32}_{\text{coarse}}$	coarse-grid convergence index	—
h	specific enthalpy	$\frac{\text{kgm}^2}{\text{s}^2}$
h	representative grid cell size for the GCI-study	—
h_1	representative grid cell size of the fine mesh	—
h_2	representative grid cell size of the medium mesh	—
h_3	representative grid cell size of the coarse mesh	—
h_{BN}	height of the secondary nozzle elevations	m
Δh_{BN}	height of the central secondary nozzle elevation	m
Δh_{main}	height of the central main engine elevation	m
h_t	total enthalpy	$\frac{\text{kg m}^2}{\text{s}^2}$
k_f^b	backwards reaction rate	—
k_f^f	forwards reaction rate	—
M	Mach number	—
M_e	exit Mach number	—
$\text{M}_{\text{BN, e}}$	exit Mach number of the RET-1S bleed nozzles	—
M_s	molar mass of species s	$\frac{\text{kg}}{mol}$
$\dot{m}_{\text{BN,ref}}$	bleed nozzle mass flow reference case Sippel et al.[35]	$\frac{kg}{s}$
$\dot{m}_{\text{BN,RET}}$	RET-1S bleed nozzle mass flow	$\frac{kg}{s}$
$\dot{m}_{\text{GG,ref}}$	gas generator mass flow reference case Brossel et al.[3]	$\frac{kg}{s}$
$\dot{m}_{\text{main,ref}}$	main engine mass flow reference case Sippel et al.[35]	$\frac{kg}{s}$
$\dot{m}_{\text{main,RET}}$	RETALT1 main engine mass flow	$\frac{kg}{s}$
$\frac{\text{O}}{\text{F}}$	oxidizer to fuel ratio	—
N	number of cells used for the GCI computation	—
N_1	number of grid cells for the fine mesh	—
N_2	number of grid cells for the medium mesh	—
N_3	number of grid cells for the coarse mesh	—
N_{BN}	number of active bleed nozzles during the ascent phase in hte half model	—
N_{main}	number of active main engines during the ascent phase in hte half model	—
n	temperature exponent	—

Variable	Definition	Unit
n_s	molar density of species s	$\frac{\text{mol}}{\text{m}^3}$
p	apparent order of the Richardson extrapolation	$-$
P	turbine power of Vulcain engine	W
P	pressure	bar
P^*	total pressure	bar
P_c	total pressure in the combustion chamber	bar
P_e	exit pressure	bar
P_{in}	turbine gas inlet pressure	bar
P_{out}	turbine gas outlet pressure	bar
$\overline{q}_{\text{ATDB}}$	reference mean base heat flux for the Aerothermal Database by Laureti et al. [23]	$\frac{\text{kW}}{\text{m}^2}$
$\overline{q}_{\text{BN off, ASC}}$	mean base heat flux for deactivated bleed nozzles during the ascent	$\frac{\text{kW}}{\text{m}^2}$
$\overline{q}_{\text{BN off, DEC}}$	mean base heat flux for deactivated bleed nozzles during the descent	$\frac{\text{kW}}{\text{m}^2}$
$\overline{q}_{\text{BN on, ASC}}$	mean base heat flux for active bleed nozzles during the ascent	$\frac{\text{kW}}{\text{m}^2}$
$\overline{q}_{\text{BN on, DEC}}$	mean base heat flux for active bleed nozzles during the descent	$\frac{\text{kW}}{\text{m}^2}$
$q(p)$	improvement factor for irregular grid refinement	$-$
R	specific gas constant	$\frac{\text{J}}{\text{kg K}}$
r	refinement factor in the GCI-study	$-$
r_{21}	refinement factor of the medium and fine mesh	$-$
r_{32}	refinement factor of the coarse and medium mesh	$-$
$r_{\dot{m}}$	mass flow ratio	$-$
r_{sup}	supersonic area ratio	$-$
s	correction factor for the calculation of the apparent order of the Richardson extrapolation	$-$
T	temperature	K
T^*	total temperature	K
$\vec{T}_{\text{1st}}$	RETALT1 first stage thrust	kN
$\vec{T}_{\text{2nd}}$	RETALT1 second stage thrust	kN
$T_{\text{BN,e}}$	bleed nozzle exit temperature	K
T_e	exit temperature	K

Variable	Definition	Unit
T_{in}	turbine gas inlet temperature	K
T_{out}	turbine gas outlet temperature	K
T_c	total temperature in the combustion chamber	K
u	velocity	$\frac{m}{s}$
$u_{\text{BN,e}}$	bleed nozzle exit velocity	$\frac{m}{s}$
u_e	exit velocity	$\frac{m}{s}$
u_t	throat velocity	$\frac{m}{s}$
V_i	volume of the ith volume cell in the GCI-study	$-$
w_s	change rate of the species s	$-$
y^+	dimensionless wall distance	$-$

Greek letters

Variable	Definition	Unit
α_s^r	stoichiometric coefficient for the educt	$-$
β_s^r	stoichiometric coefficient for the product	$-$
ϵ_{21}	difference of the charateristic flow variable between the medium and fine mesh	$-$
ϵ_{32}	difference of the charateristic flow variable between the coarse and medium mesh	$-$
γ	heat capacity ratio	$-$
ρ	density	$\frac{\text{kg}}{\text{m}^3}$
ρ^*	total density	$\frac{\text{kg}}{\text{m}^3}$
ρ_c	density inside the combustion chamber	$\frac{\text{kg}}{\text{m}^3}$
ρ_e	exit density	$\frac{\text{kg}}{\text{m}^3}$
ρ_{in}	turbine gas inlet density	$\frac{\text{kg}}{\text{m}^3}$
ρ_{out}	turbine gas outlet density	$\frac{\text{kg}}{\text{m}^3}$
ρ_t	throat density	$\frac{\text{kg}}{\text{m}^3}$
ϕ_1	characteristic flow variable on the fine mesh	$-$
ϕ_2	characteristic flow variable on the meidum mesh	$-$
ϕ_3	characteristic flow variable on the coarse mesh	$-$
ϕ_{ext}^{21}	extrapolated value between the medium and fine mesh	$-$

Variable	Definition	Unit
ϕ_{ext}^{32}	extrapolated value between the coarse and medium mesh	−

Abbreviations

Abbreviation	Definition
ACS	Aerodynamic Control Surfaces
ASME	American Society of Mechanical Engineering
AUSMDV	Advection Upwind Splitting Method, Flux Vector and Flux Difference splitting biased
ATDB	Aerothermal Database
CFD	Computational Fluid Dynamics
DLR	Deutsches Zentrum für Luft- und Raumfahrt
DRL	Downrange Landing
GCI	Grid Convergence Index
GF	Grid Refinement
GTO	Geostationary Transfer Orbit
LEO	Low Earth Orbit
LH$_2$	Liquid Hydrogen
LOx	Liquid Oxygen
MECO	Main Engine Cut Off
RANS	Reynolds-Averaged Navier-Stokes Equations
RET-1S	Vehicle-Designation: Retro-Propulsion 1st Stage
RETALT	Retro-Propulsion Assisted Landing Technologies
RTLS	Return to Launch Site
SA	Spalart-Allmaras
SSTO	Single Stage To Orbit
TSTO	Two Stage To Orbit
VTVL	Vertical Take-off, Vertical Landing

1. Introduction

Reusable launch vehicles (RLVs) have the potential to be a resource- and cost-efficient alternative for conventional space transport systems. The idea of reusing parts of the vehicle or the entire system exists since the last century ([22]) and had a peak in interest during the application of the Space Shuttle [32]. However, due to the high complexity of the vehicle and the corresponding refurbishment costs, the Space Shuttle program was shut down for economical reasons.

With the successful recovery of the Falcon9 first stage [6], showing the feasibility of Vertical Take-off Vertical Landing (VTVL) launch vehicles, the demand for RLVs is increasing again. Several actors in the sector of space transportation are currently in the maturing process of RLVs with the intention of applying them as the first stages of their launchers, including Rocket Lab with Neutron [4]. Additionally, the European long term strategy aims towards the development and characterization of RLV relevant technologies for their next generation of launchers [31]. Among these projects is the EU funded Retro Propulsion Assisted Landing Technologies (RETALT) vehicle [25].

A major aspect during the design process of an RLV is the correct dimensioning of the Thermal Protection System (TPS) in order to avoid critical failure of the vehicle. Therefore, the precise prediction of the aerothermal loads acting on the launch vehicle along the entire flight trajectory is required. Critical values of the thermal loads on the vehicle structure can mainly be identified on the aerodynamic control surfaces, landing legs and baseplate. During the propelled flight phases, the thermal loads in the aft-bay region and therefore on the baseplate are dominated by the exhaust plume structure of the main engines. Due to strong plume-plume interaction of the main engine exhaust for increasing altitudes, the hot exhaust gas is entrained towards the baseplate of the vehicle. These plume-plume interactions and the resulting base flow of clustered main engines in conventional space transport systems have been studied for several decades [9], [29], [28]. Since the ascent trajec-

tory is essentially the same for RLVs and conventional space transport systems until MECO and stage separation, the observed flowfield characteristics are also present in VTVL configurations of an RLV. Additionally, in the work of Mehta et al. [28] the influence of the base flow structures on the heat flux characteristics along the vehicle baseplate were investigated in detail.

Owing to the changed flow conditions during the return phase of the vehicle and especially during the retro-propulsion phase, new challenges in the characterization of the aerothermal loads arise. During the retro-propulsion maneuver, the counterflowing jets against the free stream velocity vector lead to an immersion of the vehicle in the hot main engine exhaust, causing high thermal loads on the rocket structure. These thermal loads were identified in previous studies by Laureti et al. [23], Ecker et al. [10] and Zilker [44]. However, in both cases, for conventional space transport systems and RLVs, the influence of additional fuel outflow from secondary nozzles in open liquid rocket engine cycles on the base flow characteristics and heat flux distribution were not considered. The secondary exhaust gas, which contains unburned hydrogen, is used to power the oxidizer and fuel pumps of the main engines [35], [3] and is ejected near the high temperature main engine exhaust. Our concern is, that the ejection of the unburned hydrogen near the high temperature main engine exhaust could lead to a post-combustion of the fuel rich mixture. This might lead to a significant increase of the thermal loads along the vehicle baseplate.

In order to fill this knowdledge gap and to provide an assessment of the additional influence of the secondary exhaust jets on the aerothermal loads acting along the vehicle baseplate, steady-state CFD simulations were carried out for representative points along the flight trajectory of an RLV. The geometry, main engine and free stream conditions are based on a simplified version of the already mentioned RE-TALT1 first stage, which is a close approximation of the Falcon9 vehicle. In order to provide an overview of the mission plan and the vehicle characteristics in general, a short description will be given in the following section.

Thesis Structure and Overview

Apart from the *first chapter* of this thesis, given by the introduction, the work consists of four more chapters.
The *second chapter* is devoted to the theoretical descriptions required for the ba-

sic understand of this work. A small overview on the functionality of liquid rocket engine cycles and the formation of supersonic exhaust jets of single nozzles and clustered main engines will be given.

The *third chapter* covers the numerical setup of the observed launch vehicle. A description of the numerical settings of the applied flow solver (DLR TAU code), the computational domain, mesh and the boundary conditions will be provided. The main aspect of the chapter is the estimation of the boundary conditions for the additional fuel outflow from secondary nozzles. Additionally the validity of the generated numerical mesh will be confirmed in a grid convergence study.

The *fourth chapter* discusses the numerical results, explains the observed flowfield characteristics and provides an assessment of the aerothermal loads due to the secondary exhaust flow.

Finally, the *fifth chapter* summarizes the results and draws conclusions from them, concerning the influence of the cold gas outflow from secondary nozzles. An outlook on the focus of subsequent studies will be given.

Disclaimer: Additional publication

Parts of this work, including the numerical setup in sec. 3 and the results for the ascent trajectroy in sec. 4 have already been published in a conference paper by the author [15], literally and figuratively. The results of the master thesis were presented at the European Aerospace Conference (EUCASS) 2023 and the publication can be found in the proceedings of the conference.

1.1. RETALT1 vehicle characteristics and mission plan

All simulations for the assessment of the aerothermal loads acting on a reusable launch vehicle (RLV) with additional bleed nozzle and gas generator outflow in this work are based on a simplified version of the RETALT1 first stage without the aerodynamic control surfaces and landing legs. Therefore, to provide a certain context of the project, the general structure and characteristics of the vehicle, as well as the overall mission plan will be briefly discussed in the following. A detailed description of the project, which provides the foundation for this section, can be found in the

1. Introduction

publications by Marwege et al. [25],[26] and Zaiacomo et al. [8].

The RETro propulsion Assisted Landing Technologies (RETALT) project is funded in context of the EU Horizon 2020 program with the goal of characterizing and developing RLV relevant technologies for Vertical Take-off Vertical Landing (VTVL) launch vehicles using retro-propulsion. Retro-propulsion denotes the concept of decelerating the vehicle during the return phase to the ground by operating the main engines against the free stream velocity vector. The research in context of RETALT is done in cooperation between the German Aerospace Center (DLR), CFS Engineering, Elecnor Deimos, MT Aerospace, Almatech and Amorim Cork Composites. As part of the project, two distinct configurations for a Single Stage To Orbit (SSTO) and a Two Stage To Orbit (TSTO) vehicle are investigated. In this work we are only focusing on the TSTO RETALT1 vehicle, which represents a state-of-the-art configuration comparable to the SpaceX Falcon 9 vehicle [6].

Instead of building a full scale demonstrator of the vehicle, the main focus of the project is to conduct numerical simulations and to validate them with representative wind tunnel tests. To speed up the development process, the already existing Vulcain 2 main engine applying a liquid oxygen (LOx) and liquid hydrogen (LH$_2$) gas generator cycle is slightly modified and used for the propulsion of the vehicle. The first stage is powered by nine engines with a central main engine and the rest being arranged in an annular shape around it, providing a thrust of $\vec{T}_{1st} = 9 \times 1179$ kN $= 10614$ kN. The second stage is powered by a single engine with $\vec{T}_{2nd} = 930$ kN. The total height of the vehicle, without main engines, is given by 103 m, while the height of the first stage without the interstage fairing equals 64.7 m. The latter value will be the reference length of the vehicle in the numerical setup. The vehicle diameter equals 6 m.

Figure 1.1.: RETALT1 vehicle concept and dimensioning by Marwege et al.[25].

Additonal information can be taken from the table in Appendix A. A schematic

visualization of the RETALT1 vehicle with characteristic length scales and stage indication can be seen in fig.(1.1).

The mission plan for the RETALT1-vehicle is to inject either a payload of 20 tons into Low Earth Orbit (LEO) or a payload of 14 tons into Geostationary Transfer Orbit (GTO). Until stage separation and Main Engine Cut Off (MECO) the operation conditions and flight trajectory is comparable to a conventional space transport system. After MECO, further acceleration of the upper stage is carried out until reaching the target orbit. For the first stage recovery two trajectories can be performed, depending on the target orbit and payload mass. While a Return To Launch Site (RTLS) trajectory is identified for the injection into LEO, the stage recovery of the GTO mission is done with a Down Range Landing (DRL) maneuver on a drone ship, which is comparable to the Falcon 9 retrieval.

In case of the RTLS, a flip over maneuver is performed directly after MECO, leading to a 180° rotation of the first stage and a boostback burn is performed to direct the vehicle back to the launch site. Another flip over maneuver has to be performed after the completion of the boostback burn to prepare the vehicle for the atmospheric reentry burn. The Aerodynamic Control Surfaces (ACS) are deployed. After the reentry of the vehicle into the denser atmosphere, three of the main engines are reignited to perform the reentry burn, followed by an aerodynamic glide phase guided by the ACS. The final trajectory phase is given by the landing burn, where only the central main engine is operated and the landing legs are deployed
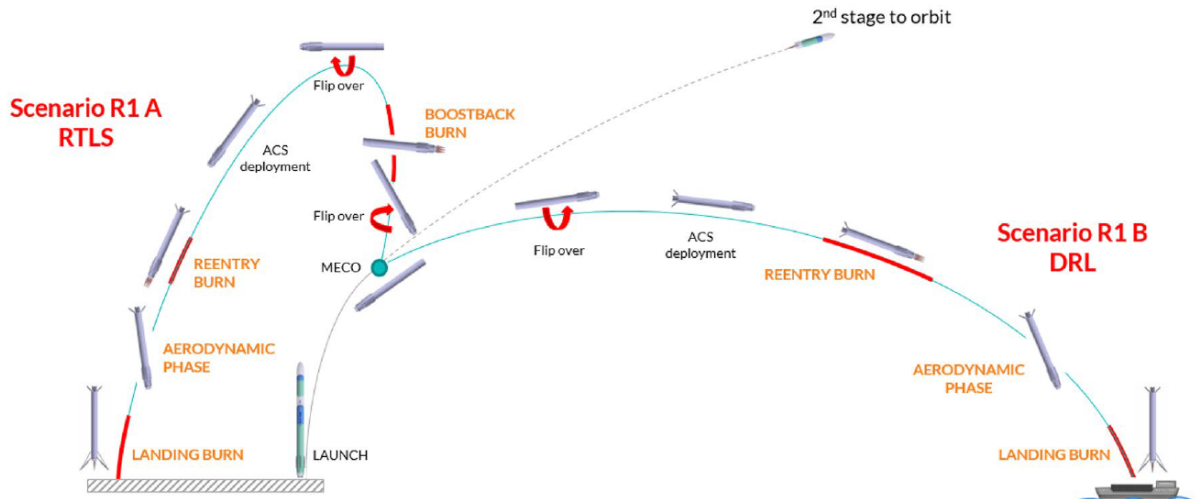
Figure 1.2.: RETALT1 mission plan and first stage return concept published by Zaiacomo et al.[8].

for the touch down. The same maneuvers are employed during the DRL without the first flip over maneuver and boostback burn. A schematic outline of the mission trajectories can be seen in fig.(1.2).

Since the focus of this work is to characterize the flowfield and heat flux conditions for active secondary nozzle outflow in gas generator and bleed engine cycles, which are used to drive the turbines of the oxidizer and fuel pump, only flow conditions during the propelled flight phases are relevant. Therefore numerical simulations are only conducted for the Ascent and Retro-burn phase and a detailed description of the simulated trajectory points is given in sec. 3.2.1.

2. Theory

In this chapter, the functionality of the two state of the art liquid main engine cycles observed in this work will be described and the governing equations for calculating the chamber conditions of the secondary nozzles in the next chapter will be derived. Additionally the flowfield and shock characteristics of supersonic exhaust jets expanding from single nozzles and the interaction of jets emanating from clustered main engines will be explained for the ascent and retro-propulsion phase of an RLV.

Conservation Equations, Reynolds-Averaging and Turbulence Modelling

In this work we renounce to derive the fundamental conservation equations of numerical fluid dynamics (CFD), which was done in previous publications by the author [14]. For the interested reader with the desire to understand the basic principles applied in CFD-applications, a detailed description and derivation of the Reynolds- and Favre-Averaged Navier-Stokes (RANS) equation can be found in the textbook by Wilcox [43]. The RANS-equations represent a time-averaged form of the Navier-Stokes equations. In case of compressible flows, the density fluctuations have to be considered aswell and the approach of Favre introduces density-averaged flow quantities. In both cases the same equations are solved for differently averaged quantities. Therefore, in the rest of this work we will referre to the Favre-method simply as RANS-approach.

In addition to the derivation of the conservation equation in the publication by Wilcox, the procedure for solving the closure problem of the RANS approach for the Reynolds-Stress tensor by applying the Boussinesq approximation [2] can be retraced. The Boussinesq approximation results in the formulation of linear eddy viscosity turbulence models, of which only the Spalart-Allmaras model will be used in this work [37]. The applied closure coefficients and auxiliary relations are stated in the work of Wilcox. Additionally the requirements on the grid-discritization of the boundary layer flow along walls with no-slip condition are explained for turbulence

models without the application of wall functions (e.g. Spalart-Allmaras models).

2.1. The functionality of open liquid rocket engine cycles

The following summary of the general concepts of liquid rocket engine cycles makes no claim to be complete, instead it is intended to give an overview on the applied principles in this work and to provide a better understanding of the concepts used in the sections 3.2.2-3.2.3. A detailed introduction in the fundamental concepts of liquid-propellant rocket engines is given in the publication by Veris [7] and El-Sayed [12].

In general several main engine cycles can be applied for the propulsion of space launch vehicles. However, in the following we will only focus on pump-fed, liquid rocket engine cycles. Some advantages of liquid rocket engines are the throttling capability, the mixture ratio control and the ability to shut down and restart the engine [12]. Therefore, these type of engines are the only option for the propulsion of an RLV today and enable the restart during the retro-propulsion phase.

The main components of a liquid-propellant rocket engine are the oxidizer and fuel tanks, one or multiple combustion chambers, a mechanism for delivering the reactants to the combustion chamber and the corresponding power source and the pipe-system connecting the different components. In general two major types of feed systems can be identified, the pressure-fed and pump-fed systems. In case of the pressure-fed cycle, the propellants are stored under high pressure in their tanks to guarantee the necessary chamber conditions and to deliver the reactants to the combustion chamber. Due to the avoidance of complex systems, these engine cycles represent a simple and reliable configuration. However, due to the high pressure needed for storing the oxidizer and fuel, the large corresponding mass and size of the tanks are great disadvantages. To avoid these problems a more efficient way of providing the necessary mass flow and combustion pressure is to apply turbopumps. These pumps are used to increase the pressure of the liquid propellants above the storage value for a high pressure injection into the combustion chamber [7]. The engine cycle is classified by the powering mechanism of these turbopumps. In the following two sub-sections only the gas generator cycle and the expander bleed engine cycle will be discussed. Additionally we can distinguish between an open and a closed engine cycle. In a closed cycle, the gas powering the pumps is returned

to the main combustion chamber, while it is expelled through additional nozzles in the open cycle. Since the influence of secondary nozzles on the thermal loads of a launch vehicle are investigated, only open engine cycles are considered.

Bleed Engine Cycle

In an expander bleed engine cycle, a small portion of the cryogenic hydrogen is tapped-off from the main fuel line and pumped through the cooling channels of the combustion chamber and nozzle walls, leading to a regenerative cooling of the engine. During this cooling process, the heat along the combustion chamber walls is absorbed by the cooling flow, which evaporates and expands. The heated gas is used to drive the oxidizer and fuel pumps, which are connected to the turbopumps through a shaft. Instead of joining the coolant flow with the main fuel line and burning it in the combustion chamber, the exhaust gas is expelled in secondary nozzles. Therefore, the pressure of the fluid leaving the turbines does not have to be greater than the pressure in the combustion chamber. A schematic visualization of the engine cycle can be seen in fig.(2.1 (a)).

Gas Generator Cycle

Instead of using the thermal expansion of the cooling flow through the nozzle and combustion chamber walls of the main engines, the gas generator cycle uses an auxiliary combustion chamber. A small amount of the propellants is tapped off of the main supply lines and burned in the secondary combustion chamber. The created exhaust gas is expanded through a nozzle and directed onto the turbine blades. To avoid structural damage of the turbine, a fuel rich mixture is burned in the combustion chamber, leading to an exhaust gas mixture with temperatures below the melting point of the applied metals. These turbines are used to power the oxidizer and fuel pumps and are connected to them through a shaft. After leaving the turbine, the exhaust gas is expanded through a nozzle and expelled in the ambient air. During the start-up sequence of both engine cycles, the expander bleed engine cycle and the gas generator cycle, the required chamber conditions and nozzle wall temperatures are not sufficient to power the turbines for the oxidizer and fuel pump. Therefore, alternative methods must be applied for these conditions, for example cold gas thrusters. A schematic visualization of a gas generator cycle with regenerative cooling and two separate secondary nozzles for the exhaust gas of the oxidizer and fuel pump can be seen in fig.(2.1 (b)).
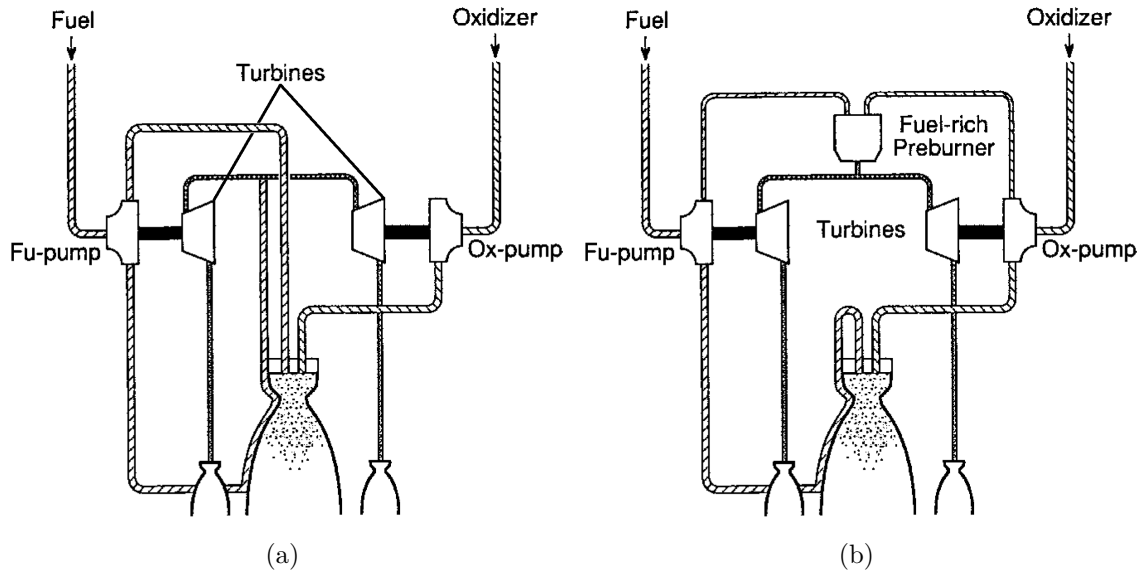
Figure 2.1.: Schematic visualization of the (a) expander bleed engine and (b) gas generator cycle based on Manski et al. [24] and modified.

2.2. The flow and gas expansion through an axisymmetric nozzle

In this section the equations for characterizing the relevant flow parameters through an axisymmetric nozzle, including the temperature, density and pressure will be derived. The theory in this section is based on the publications by Veris [7], Klinkov [21] and Ganzer [17].

For the derivation of the equations connecting the combustion chamber conditions with the outflow conditions of the supersonic nozzle the following assumptions are made:

- the flow through the nozzle is isentropic and therefore adiabatic and frictionless,

- the gas flow is assumed to be one-dimensional, meaning, that the state variables only change in one direction,

- the flow is compressible and therefore the density of the observed fluid can change with the pressure,

- the flow velocity in the combustion chamber is small and therefore negligible

compared to the velocity through the nozzle and in the exit plane,

- the flow is assumed to be stationary,

- the fluid expanding through the nozzle is described by the perfect gas equations of state.

The last assumption allows the usage of the ideal gas law given by [7]:

$$P = \rho R T, \tag{2.1}$$

where P is the pressure, ρ the density of the fluid, R the specific gas constant and T the temperature. Additionally, the specific gas constant, ratio of specific heats and the internal energy of a perfect gas are defined as [17]:

$$R = c_p - c_v, \tag{2.2}$$

$$\gamma = \frac{c_p}{c_v}, \tag{2.3}$$

$$e = c_v T, \tag{2.4}$$

with the specific heat capacity for constant pressure c_p and constant volume c_v. This assumption is valid due to the relatively low temperatures and the constant values of the specific heat capacities, ratio of specific heats and specific gas constant.
The equation for the conservation of energy for a stationary, one dimensional flow in the integral form is given by [17]:

$$e + \frac{u^2}{2} + \frac{P}{\rho} = \text{const.} \tag{2.5}$$

with u being the velocity of the flow. Together with the specific enthalpy, which is defined as [17]:

$$h = e + \frac{P}{\rho}, \tag{2.6}$$

the energy equation can be rewritten as:

$$h + \frac{u^2}{2} = h_t = \text{const.} \tag{2.7}$$

2. Theory

By using the definition of the internal energy for a perfect gas and by introducing the speed of sound [17]:

$$c^2 = \left(\frac{\partial p}{\partial \rho}\right) = \gamma \frac{P}{\rho} = \gamma R T, \tag{2.8}$$

the specific enthalpy can be expressed in terms of the speed of sound as:

$$h = e + \frac{P}{\rho} = c_v T + R T = c_p T = \frac{c_p}{\gamma R} c^2 = \frac{c^2}{\gamma - 1}. \tag{2.9}$$

This definition of the specific enthalpy together with eq.(2.7) and the assumption, that the flow velocity in the reservoir is negligible, leads to the following formulation of the energy equation for an ideal gas [17]:

$$c^2 = \frac{\gamma - 1}{2} u^2 = c_0^2, \tag{2.10}$$

$$\frac{c_0^2}{c^2} = 1 + \frac{\gamma - 1}{2} M^2, \tag{2.11}$$

with $M = \frac{u}{c}$ being the Mach number. In this work the inflow reservoir is given by the combustion chamber of the nozzle.

In the following, the relation between the the total temperature T^*, total pressure P^* and total density ρ^* and their corresponding state variable will be derived from the energy equation of the ideal gas. The relation for the temperature can be derived by simply plugging the definition of the speed of sound into eq.(2.11), leading to [17]:

$$\frac{T^*}{T} = 1 + \frac{\gamma - 1}{2} M^2. \tag{2.12}$$

To rewrite this equation in terms of the pressure and density, the isentropic relations are used [17]:

$$\left(\frac{\rho^*}{\rho}\right)^\gamma = \frac{P^*}{P} = \left(\frac{T^*}{T}\right)^{\frac{\gamma}{\gamma - 1}}, \tag{2.13}$$

resulting in the following equations [17]:

$$\frac{P^*}{P} = \left[1 + \frac{\gamma - 1}{2} M^2\right]^{\frac{\gamma}{\gamma - 1}}, \tag{2.14}$$

$$\frac{\rho^*}{\rho} = \left[1 + \frac{\gamma - 1}{2} M^2\right]^{\frac{1}{\gamma - 1}}. \tag{2.15}$$

Finally, by using the continuity equation [17]:

$$\rho_e A_e u_e = \rho_t A_t u_t \qquad (2.16)$$

with the index e denoting the exit conditions of the nozzle and index t the throat conditions and using the isentropic relations stated above, the area ratio between the nozzle exit and throat can be rewritten in relation to the exit Mach number, leading to [21]:

$$\frac{A_e}{A_t} = \frac{1}{M_e^2} \left[\frac{1 + \frac{\gamma-1}{2} M_e^2}{\frac{\gamma+1}{2}} \right]^{\frac{\gamma+1}{2(\gamma-1)}}. \qquad (2.17)$$

These equations for the temperature, pressure and density ratio will be used in sec. 3.2.2 and sec. 3.2.3 to derive the chamber conditions of the bleed nozzle and gas generator, respectively. Additionally the equation for the area ratio is used to derive the nozzle throat diameter for a generic nozzle contour used to simulate the outflow of the bleed nozzle and gas generator with the derived chamber conditions in sec. 3.2.4.

2.3. The formation and characteristics of supersonic free jets

After the expansion of the gas through the axissymmetric nozzle, the exhaust is expelled into the ambient air. Since the nozzle outflow velocities of the RETALT1-vehicle are in the supersonic regime, only the characteristics of supersonic exhaust jets will be discussed. Therefore it is assumed, that the flow inside the nozzle and through the exit plane, from which the exhaust jets are emanating, is fully supersonic. Under this assumptions, a phenomenological description of the flowfield characteristics and shock structure of supersonic, axisymmetric exhaust jets formed by a generic nozzle will be given based on the specifications made in the publications by Klinkov [21] and Feldner [14].

By introducing the expansion ratio, or degree of off-design [21], relating the exit pressure to the ambient pressure in the observed nozzle configuration:

$$r_{\text{exp.}} = \frac{P_e}{P_a}, \qquad (2.18)$$

the supersonic exhaust jets can be divided into underexpanded ($r_{\text{exp.}} > 1$), ideally-expanded ($r_{\text{exp.}} = 1$) and overexpanded ($r_{\text{exp.}} < 1$) jets. The exhaust jet structure of slightly underexpanded and overexpanded nozzle outflow is given in fig.(2.2).

<table>
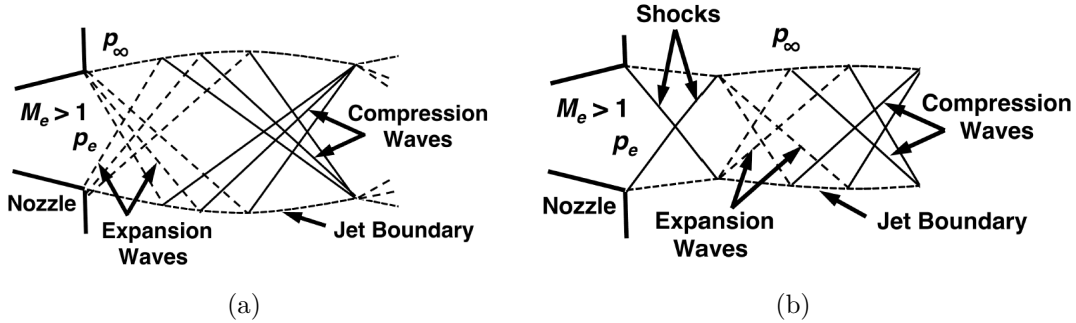<tr><td>(a)</td><td>(b)</td></tr>
</table>

Figure 2.2.: Visualization of the exhaust jet structure of a) slightly underexpanded jets. The compression waves are not converging towards the central jet region and no formation of a nozzle shock is observed. b) overexpanded nozzles. This graphic is taken from the work of Zilker [44].

First we will consider the case of underexpanded jets and therefore a configuration, where the nozzle exit pressure is higher than the ambient pressure. Due to the non-ideal expansion of the exhaust flow, a centered expansion fan forms at the nozzle outlet, which is normally reflected at the symmetry axis of the jet. The flow passing through the expansion waves of the expansion fan is deflected in outwards direction, leading to an increase of the cross-sectional jet area downstream of the nozzle exit, until a local maximum is reached. A negative curvature of the jet boundary is observed. The high velocity gradient between the exhaust jet and the ambient air leads to the formation of a shear layer, which can be described by a continuous distribution of infinitesimal, tangential discontinuities of the entropy, so called slip lines or slip surfaces. In case of tangential discontinuities, the velocity component in normal direction disappears ($u_\perp = 0$), preventing the flow through the slip lines. This definition, together with the negative curvature of the jet boundary and a constant static ambient pressure, leads to the reflection of the incoming expansion waves, which were already reflected at the symmetry axis, as converging compression waves and their intersection. The formation of an oblique shock at the intersection of the compression waves, a so called nozzle shock, is observed. The formation of the nozzle shock is not observed for slightly underexpanded jets. In this case, the compression waves are not converged in the central jet region and do not intersect. This nozzle shock extends towards the symmetry axis of the jet and the shock in-

tensity increases. For moderately underexpanded jets a regular reflection of the incident shocks is observed. A contact discontinuity τ forms between the reflected shocks and separates the flow field. However, for an increasing pressure ratio and therefore highly underexpanded jets, the angle of the incident shocks and the shock intensity increase rapidly, so that a regular reflection is not possible. This results in an irregular reflection of the shock and the formation of a triple shock structure [16]. The triple shock structure consists of the incident shock σ_e, the reflected shock σ_r and the main shock σ_h, which is referred to as Mach disk. In the triple point, where the 3 shocks intersect, a tangential discontinuity τ forms again, separating the flow behind the reflected and main shock.

In both cases, the flow passing through the incident and reflected shock remains supersonic. The positive radial velocity leads to an expansion of the jet, while the flow behind the Mach disk is decelerated to subsonic velocities. For the irregular reflection, a mixing layer forms between the peripheral region of the jet and the flow behind the Mach disk, causing the transfer of momentum and the acceleration of the fluid to supersonic velocities.

Eventually the reflected shocks reach the shear layer of the jet boundary and cause the formation of a centered expansion fan. The previously described flow field observations repeat, leading to the formation of the characteristic shock cells of supersonic jets, also called shock diamonds. The total pressure behind each shock is reduced, leading to a decrease in shock intensity. When the total jet pressure equals the ambient pressure, the flow becomes shockless [14], [21]. A visualization of an underexpanded jet with irregular shock reflection at the symmetry axis is given in fig.(2.3).

If the underexpansion ratio is increased even further, the formation of a single shock cell with a curved Mach disk is observed. The spatial extend of the plume increases and instead of the oblique nozzle shock a barrel shock forms, separating the inner core of the plume from the flow in the region of the jet boundary. Again a shear layer extends along the contact surface of the exhaust plume and the ambient air. A schematic visualization of this phenomenon is given in fig.(2.4).

For ideally expanded exhaust jets $r_{\text{exp.}} = 1$ with the nozzle exit pressure being equal to the ambient pressure only a weak discontinuity forms along the nozzle outlet and a shear layer separates the jet from the surrounding fluid. The jet diameter is constant and no further expansion is observed. With increasing distance to the nozzle exit mixing of the ambient air with the potential core of the jet occurs, leading to a
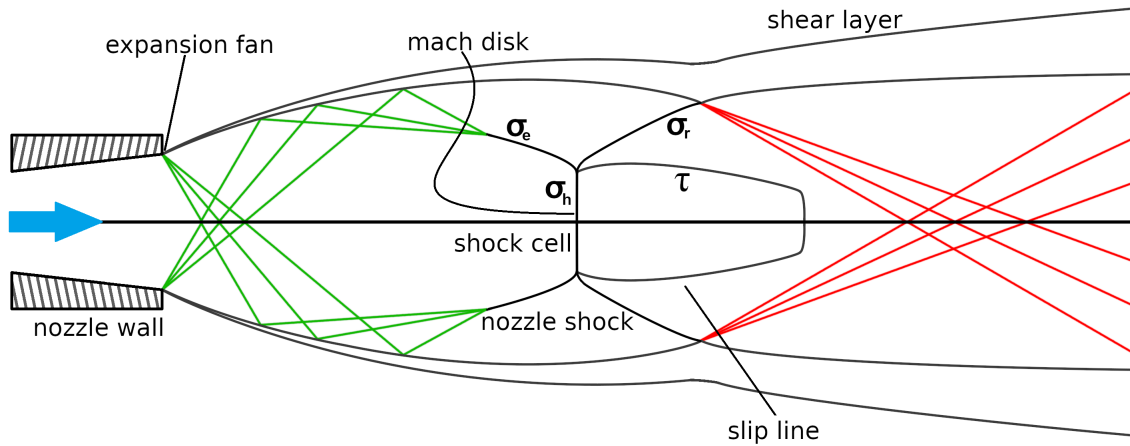
Figure 2.3.: Schematic visualization of an underexpanded exhaust jet system with irregular shock reflection. The formation and reflection of the expansion fan is indicated and the picture was taken from Feldner [14].
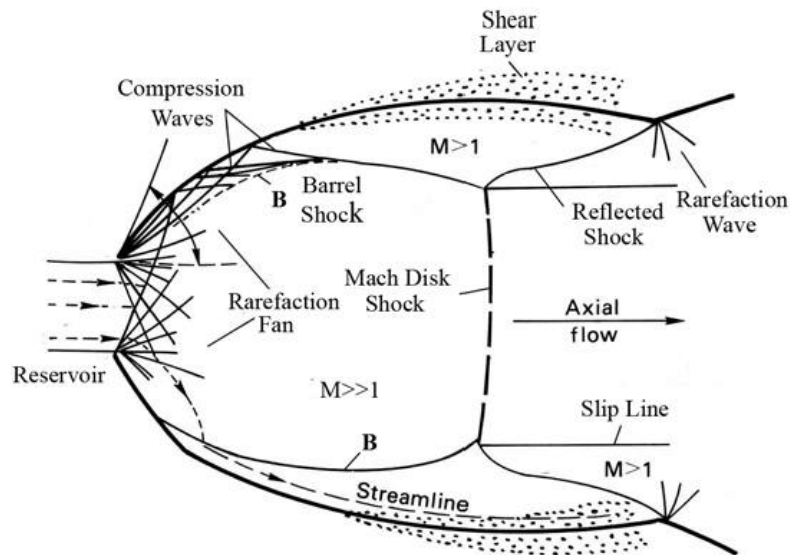
Figure 2.4.: Schematic visualization of an extremely underexpanded exhaust jet system with a single shock cell and the formation of a barrel shock taken from van Donkelaar [41].

reduction of the exhaust velocity [44],[1].

In case of overexpanded jets $r_{\mathrm{exp.}} < 1$, instead of the expansion fan, an overexpansion shock forms directly at the nozzle exit. The overexpansion shock raises the exit pressure of the jet to the ambient pressure of the surrounding fluid, since no pressure gradients are possible across the jet shear layer. The periodic compression

and expansion of the jet and the formation of shock cells, previously described for underexpanded jets, is observed again.

Owing to the varying ambient pressure during the flight trajectory of a launch vehicle, the expansion ratio constantly changes. For the simulated trajectory points and observed altitudes in this work the main engine exhaust of the RETALT1 vehicle is underexpanded. Due to the smaller exit pressure of the secondary nozzles, the resulting exhaust jets are overexpanded for the first simulated trajectory point and underexpanded for the remaining altitudes.

2.4. Plume formation of clustered nozzle arrays

In the previous section, the flowfield and shock characteristics of an exhaust jet emanating from a single nozzle were described for varying exit pressures. However, in order to generate the desired thrust conditions in modern launcher configurations, the first stage generally applies an array of clustered main engines. For increasing altitudes and underexpansion ratios of the nozzles, the spatial extend of the exhaust plumes increases, leading to the interaction of the single jets and strong plume-plume interactions can be observed.

Various studies of these plume-plume interactions applying an arrangement of two [9], four [30],[29] and six main engines [28] were conducted for the ascent phase of launch vehicles and some of them were summarized in the thesis of Zilkner [44]. Additonally the work by Zilkner includes the theoretical explanation of the exhaust plume structure of an RLV during the retro-propulsion phase with three of the nine main engines active. Similar to the RETALT1 vehicle the active engines are in line along the symmetry axis of the computational domain. Therefore, based on the previously mentioned publications, a description of the shock and flowfield characteristics formed by an array of main engines will be given for the ascent and retro-propulsion phase of an RLV in the following two sections.

2.4.1. Shock structure of nozzle arrays during the ascent of a launch vehicle

The flowfield in the aft-bay region of a launch vehicle during the ascent phase is characterized by a wide regime of flow conditions and high gradients of the velocity

and temperature. A visualization of the occurring phenomena and shock formations for moderately and highly underexpanded exhaust jets during this flight phase can be seen in fig.(2.5). In the following description the main engine thrust is assumed to be constant along the flight trajectory.
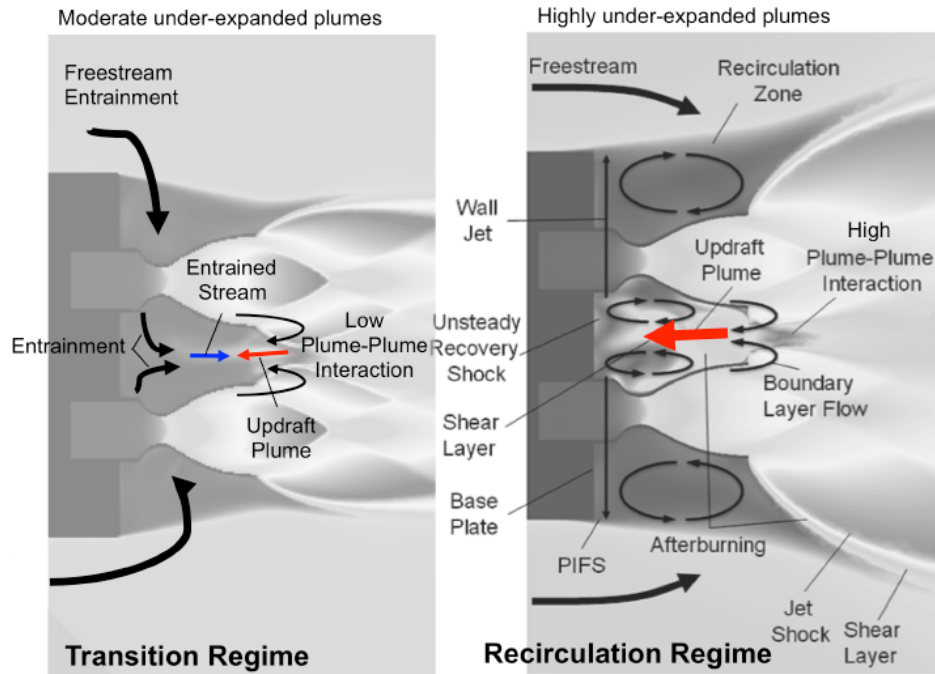

Figure 2.5.: Schematic visualization of the flow in the aft-bay region during the ascent phase taken from Mehta et al.[28].

For moderately underexpanded jets, the expansion of the exhaust gas downstream of the nozzle exit leads to the impingement and interaction between adjacent jets, causing the formation of oblique shocks and a stagnation point at the intersection. A negative pressure gradient against the main engine flow direction forms. Gas flow with lower velocities and axial momentum is unable to overcome this pressure gradient and is redirected in the opposite direction, leading to a backflow of the exhaust gas towards the baseplate. This recirculating flow between the main engine outlets is referred to as updraft plume. For the transition case, the incoming free stream, due to the vehicle movement, is entrained towards the baseplate and collides with the updraft plume. The total value of the axial velocity component is equal between the updraft plume and the entrained free stream, preventing the impingement of the reverse jet onto the baseplate.

For an increasing altitude and therefore highly underexpanded operating conditions of the main engines, the plume-plume interactions and the observed pressure gradi-

ent at the stagnation point increase. A larger amount of the boundary layer flow is unable to overcome the pressure gradient and the mass flow of the updraft plume increases. The updraft jet impinges onto the baseplate, leading to the formation of a wall jet and a redirection of the flow in radially outwards direction, preventing the entrainment of the incoming free stream. Recirculation regions of the hot main engine exhaust form in between the main engines, the so called main engine cavities, and in the peripheral region of the baseplate, leading to plume-induced flow separation (PIFS). For increasing pressure ratios and mass flows of the updraft plume, a choked condition can be identified, where the velocities of the recirculating gas can reach supersonic speeds and the maximum pressure and heat flux values are observed and become independent of the ambient pressure.

2.4.2. Shock structure of counterflowing jets during retro-propulsion

During the retro-propulsion maneuver, the three main engines along the symmetry plane are operated against the incoming free stream velocity vector. Both the free stream and main engine exhaust velocities are supersonic. A visualization of the observed flowfield phenomena for a launcher, which is comparable to the RETALT1-vehicle, is given in fig.(2.6).

Due to the reflection and intersection of the expansion waves originating along the main engine outlets, a barrel shock forms downstream of the nozzles and terminates in a Mach disk. The flow passing the strong shock, given by the Mach disk, is decelerated to subsonic velocities, while the flow through the weaker barrel shock remains in the supersonic regime. The counterflowing exhaust jets combined with the vehicle geometry represent an effective obstruction for the incoming free stream and a bow shock forms downstream of the Mach disk. This leads to the creation of a stagnation region between the two shock structures, separating the exhaust plume from the incoming flow along the contact surface. The stand-off distance of the bow shock and the spatial extend of the exhaust plumes depend on the thrust conditions of the main engines and the underexpansion ratio and therefore decrease with decreasing altitude.

Owing to the interaction of the fluid passing through the barrel shock and Mach disk with the flow through the bow shock, flow deflection of the main engine exhaust towards the vehicle is observed. The high velocity gradient between the supersonic
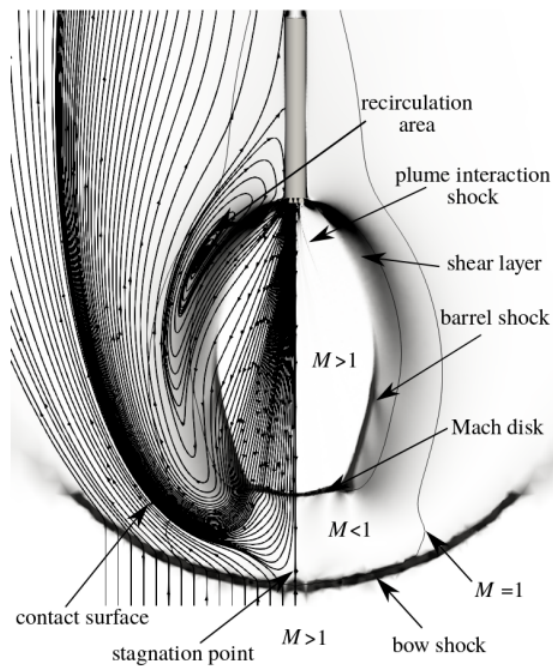
Figure 2.6.: Exhaust plume structure of counterflowing jets in RLV configurations taken from Ecker et al.[10].

exhaust jets and the flow in the stagnation region leads to the formation of a shear layer along the jet boundary. A strong, torus shaped recirculation region forms around the low pressure aft-bay and extends along the shear layer of the exhaust jets. The deflected flow impinges onto the side-walls of the vehicle, which leads to an immersion of the launcher in the hot main engine exhaust.

3. Numerical setup

The numerical setup of the DLR TAU code used for 3D simulations of a reusable launch vehicle will be described in this section. Additionally, the boundary conditions will be given, including the free stream conditions for the simulated trajectory points. A detailed description of the numerical mesh and the methods for improving the resolution of the exhaust jets and the flowfield in the aft-bay region of the vehicle will be provided. The arrangement of the secondary nozzles is presented. The derivation of the bleed nozzle and gas generator chamber conditions is explained in detail and the results of 2D axisymmetric nozzle simulations using the chamber conditions to create the nozzle outflow in the 3D simulations of the RLV are given. Concluding this chapter, the validity of the computational mesh is confirmed by conducting a grid convergence study for representative field and baseplate variables and the numerical uncertainties are reported.

3.1. DLR TAU code and numerical settings

The DLR TAU code [34] is a second-order finite-volume flow solver for 2D and 3D problems on hybrid structured-unstructured meshes. TAU uses an edge-based dual-cell approach based on a vertex-centered scheme.

In order to generate comparable results to the already existing aero-thermal database, the Reynolds-Averaged Navier-Stokes (RANS) equations together with the one-equation Spalart-Allmaras linear eddy viscosity turbulence model [37] are used for steady simulations of the flowfield. This turbulence model yields satisfactory results for the exhaust plume structure of RLVs during their flight trajectory[11] and is suitable for the prediction of wall heat fluxes in hypersonic flow regimes[19], while still being numerically robust [15] .

Second-order spatial accuracy is achieved by applying the AUSMDV[42] upwind flux splitting scheme and a least squares gradient reconstruction, while the temporal discretization is done with a 3-stage explicit Runge-Kutta method.

To improve the numerical accuracy for low Mach number regions, the low-Mach number variable reconstruction modification by Thornber[39] is applied.

Due to the fuel rich outflow of the main engines and secondary bleed nozzles, the potential effects of post-combustion are considered and the chemistry modelling is done by using a reduced 19-step Jachimowski mechanism[18]. This approach for the chemistry modelling applies a multispecies algorithm for the combustion in a liquid hydrogen, liquid oxygen main engine with the combustion species [H_2, H, O_2, OH, H_2O, H_2O_2, HO_2] and the species for the ambient air [O_2, N_2] [10]. The approach for modelling the rate changes of the species during the combustion is based on a finite rate chemistry model. The rate change for each species during the reaction is defined as [20]:

$$ w_s = M_s \sum_r \left(\beta_s^r - \alpha_s^r \right) \left[k_r^f \prod_s (n_s)^{\alpha_s^r} - k_r^b \prod_s (n_s)^{\beta_s^r} \right], \qquad (3.1) $$

with the index r indicating the reaction and index s indicating the species, α_s^r and β_s^r being the stoichiometric coefficients of the reaction for the educts and products respectively and k_r^b and k_r^f the backwards and forwards reaction rates. The molar mass is given by M_s and the molar density by n_s. The forward reaction rate can be calculated by using the Arrhenius law [13]:

$$ k = AT^n \exp\left(-\frac{E_a}{RT} \right), \qquad (3.2) $$

with A being the pre-exponential or frequency factor, n the temperature exponent and E_a the activation energy of the reaction. Finally, the rate constants for the backwards reaction can be calculated with the constants in the equilibrium state [13]. The transport coefficients of the simulated species were taken from the outpot of the *NASA CEA tool* [27].

3.2. Numerical setup and boundary conditions

In the following section, the numerical setup, including the geometry and boundary conditions of the computational domain, will be described.

The CAD-model of the simulated launch vehicle and the surrounding farfield was designed using *CATIA v5* [38]. *Centaur Version 14.0* [36] was used for the grid generation. *Centaur* enables the construction of structured-unstructured numerical

meshes with hexaedral- and prismatic-elements along walls, allowing high resolution of the boundary layer in this region, and tetrahedral elements inside the computational domain. The transition between these two regions is guaranteed by using pyramidal elements.

3.2.1. Simulation mesh and free stream conditions

The focus of this work is to characterize the flow structures in the aft-bay region of the launch vehicle during the ascent and retro-propulsion phase and the resulting thermal loads on the rocket baseplate. Therefore, all simulations are done using a simplified version of the RETALT1 first stage, without the aerodynamic control surfaces and landing legs on the 3D computational mesh shown in fig. 3.1. Depending on the observed case, the flowfield is simulated for a full model or a half model of the geometry with a total of 98 M and 49 M volume elements, respectively. The simulated trajectory points, including the height, Mach number and ambient pressure are given in tab. 3.1.

Table 3.1.: Simulated trajectory points and flight Mach number.

Trajectory point	height [km]	Mach number	ambient pressure [Pa]
Ascent 1	7	0.8	41060.7
Ascent 2	35	2.8	475.9
Ascent 3	60	4.5	20.3
Ascent 4	86	7.4	0.3
Decent 1	60	7.0	20.3
Decent 2	40	5.1	277.5

In order to create a realistic configuration and prevent flow disturbances for the ascent trajectory, a generic payload fairing was added on top of the vehicle. The simplified vehicle, which will just be referred to as RET-1S (RETro-propulsion 1st Stage) in the following, is enclosed by a spherical farfield mesh with a radius of $r_{\mathrm{ff}} = 280$ m, which corresponds to approximately four times the vehicle length. The large farfield radius is chosen in order to capture the full plume structure and shock formation for super- and hypersonic flight Mach numbers. The origin of the coordinate system and therefore the origin of the spherical farfield is given by the central
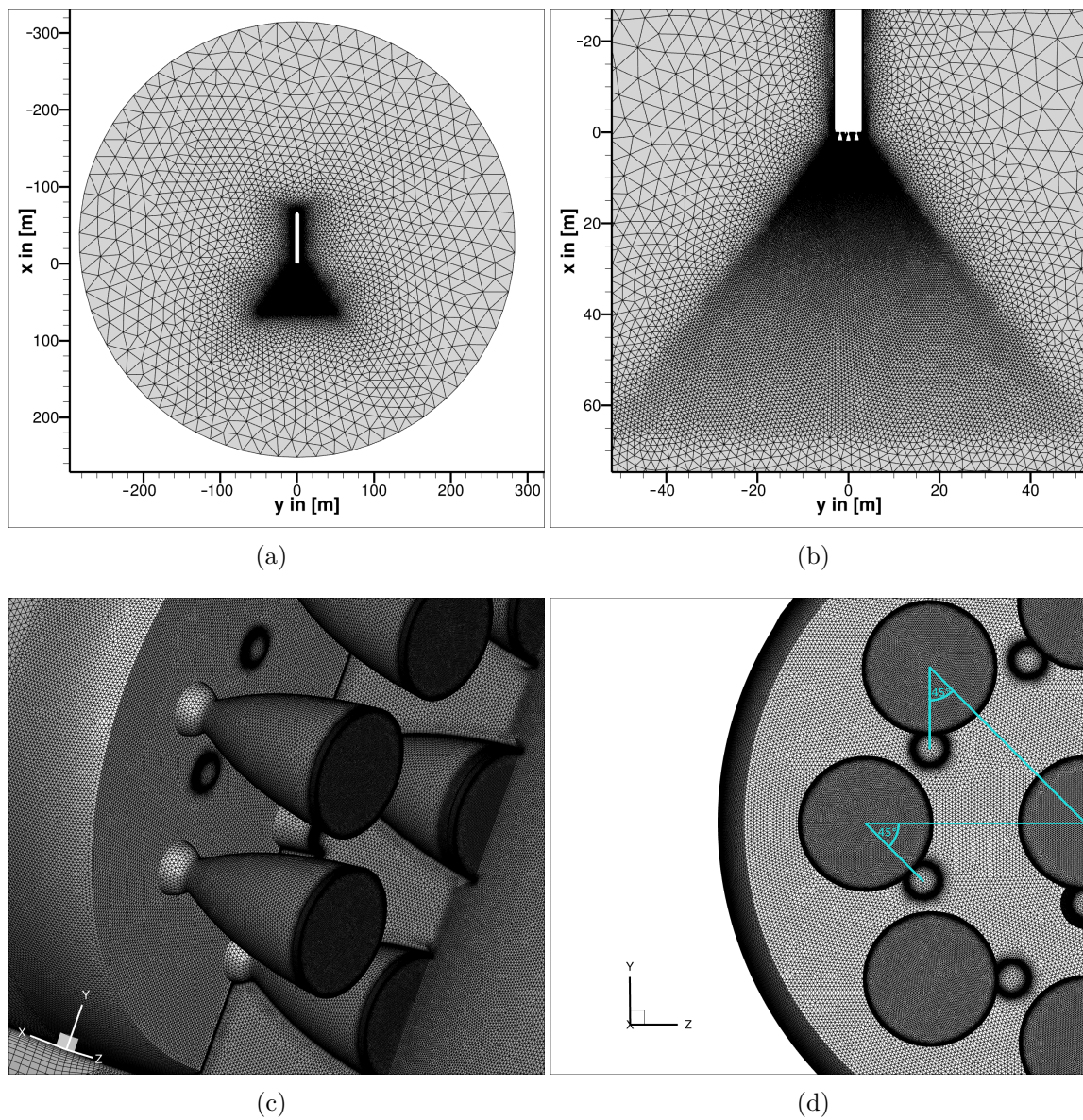
(a)

(b)

(c)

(d)

Figure 3.1.: a) View of the full mesh symmetry plane. b) Refinement region for the exhaust plume in the symmetry plane. c) 3D view on the aft-bay region of the vehicle and visualization of the main and secondary nozzles. d) Baseplate of the RET-1S-vehicle with schematic representation of the bleed nozzle arrangement.

point of the rocket baseplate.

The secondary nozzles are arranged in a ring shape between the central nozzle and the 8 outer main engines in such a way, that the angle of the line between the bleed nozzle and the nearest main engine in positive y-direction and the line between the engine with the central engine equals 45° (see fig. 1 d)). This arrangement allows to reduce the full model to a half model in the simulations of the ascent trajectory since all main engines are active during this flight phase leading to a symmetric configuration along the x-y-plane. This assumption does not hold for the descent trajectory. During this phase only the three main engines along the symmetry plane and the corresponding secondary nozzles are active. Due to the rotation of the secondary nozzles around the outer main engines, one of the secondary nozzles of the active main engines is not included in the half model and the full model has to be simulated. The secondary nozzles in the outer ring stand out from the baseplate by a height of $h_{\mathrm{BN}} = 0.03$ m. The central main engine and the secondary nozzle connected to it are elevated by $\Delta h_{\mathrm{main}} = 0.15$ m and $\Delta h_{\mathrm{BN}} = 0.4$ m. The exit diameter of the RET-1S main engines and secondary nozzles are given by $D_{\mathrm{main}} = 1.1$ m and $D_{\mathrm{SN}} = 0.14$ m, respectively. The nozzle outflow is defined by a Dirichlet boundary condition and the corresponding engine parameters will be derived in the following two sections (sec. 3.2.2, sec. 3.2.3). These boundary conditions are then used to conduct separate 2D-axisymmetric simulations of the nozzle flow in sec. 3.2.4.

To provide a high resolution of the exhaust jets while at the same time minimizing the number of implemented grid points, a cylindrical and a conical grid refinement (GF) region are applied at the aft-bay. Since the RET-1S-vehicle is aligned along the x-axis, the position of the refinement regions is fully defined by the x-coordinates of the starting point and the end point. The cylindrical refinement region is applied in between the curved aft-bay region and the outlets of the outer ring of main engines. The cylindrical refinement region is smoothly connected to the conical GF, starting at the outer main engine outlets. All relevant parameters of the two refinement regions, including the x-coordinates, the radius and the cell size at the starting position x_1 and the end position x_2 can be seen in tab.(3.2). A constant cell size is chosen for the cylindrical refinement region of the aft-bay, while the cell size for the conical refinement region increases with increasing distance to the main engine. The reason for this is, that high resolution is desired in close proximity to the baseplate and nozzle outflows to capture the dominant flow characteristics, while the relevance of the exhaust plume structure downstream of the nozzle outflow

decreases with increasing distance.

Table 3.2.: Parameters of the cylindrical and conical grid refinement regions.

Parameters	cylindrical GF region	conical GF region
x_1-coordinate in [mm]	-910	1750.6884
x_2-coordinate in [mm]	1750.6884	65000
radius 1 in [mm]	3400	3400
radius 2 in [mm]	3400	50000
cell size 1 in [mm]	30	13
cell size 2 in [mm]	30	1000

In order to guarantee the numerical accuracy of the Spalart-Allmaras turbulence model without wall functions, the first layer thickness of the boundary layer mesh is kept at small values of [0.05, 0.1] mm, which corresponds to a dimensionless wall distance of $y^+ < 1.0$.

The computational domain is initialized using a dry air species mixture with the mass fractions of $N_2 = 76.7\%$ and $O_2 = 23.3\%$. In order to generate consistent and comparable results to the aerothermal database of the RETALT1-vehicle, the isothermal wall temperature was kept at 600 K in all simulations.

3.2.2. Estimation of the bleed nozzle chamber conditions

Two main engine cycles, an expander bleed engine cycle and a gas generator cycle, were identified as suitable modelling options for the additional cold gas outflow from the secondary nozzles, as they represent two state of the art, open liquid propellant engine cycles in VTVL configurations. In both cases only little or no consistent information on detailed engine configurations with similar combustion chamber conditions combined with a description of the secondary nozzle outflow are available. Therefore the outflow conditions had to be derived by comparing and rescaling engine cycles with similar thrust and exit conditions, respectiveley. In this section, the rescaled conditions for the expander bleed engine cycle are derived for a reference engine cycle proposed in the publication by Sippel et al.[35]. In the following, we will refer to this engine cycle as BN-Sippel. A detailed visualization of the engine cycle is given in fig.(3.2). The important values for the scaling routine

have been extracted and can be taken from tab.(3.3). The general theory and functionality of an expander bleed engine cycle was described in sec. 2.1 and the equations used in this section have been introduced in sec. 2.2.
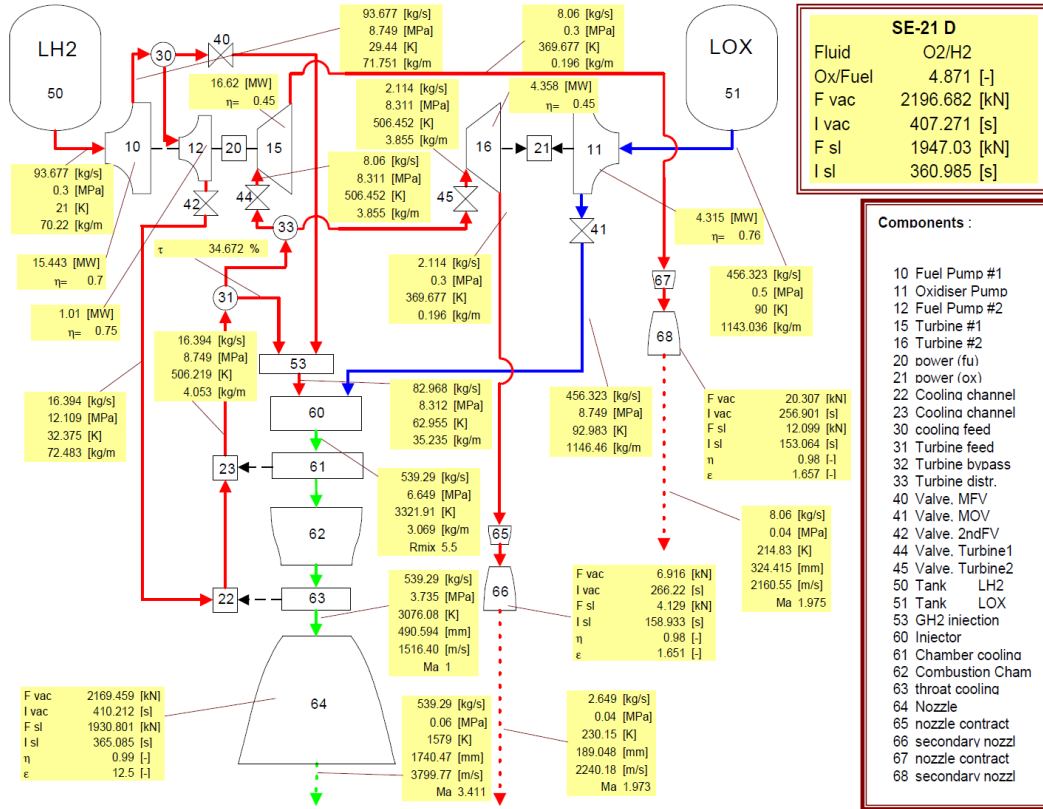

Figure 3.2.: Expander bleed engine cycle derived by Sippel et al.[35].

Table 3.3.: Reference values for the main engine and bleed nozzle outflow taken from Sippel et al.[35]

Properties	Units	Main engine	bleed nozzle 1	bleed nozzle 2
Mass flow	kg/s	539.290	2.649	8.060
Temperature	K	1579.00	230.15	214.83
Mach number	–	3.411	1.973	1.975
Exit velocity	m/s	3799.77	2240.18	2160.55
Exit pressure	bar	0.6	0.4	0.4

In the BN-Sippel cycle, the oxidizer (LOx) and fuel (LH$_2$) pumps and turbines are connected by two separate shafts and the liquid hydrogen used for powering the

pumps is ejected through two distinct bleed nozzles. Since our geometry for the RET-1S configuration only applies a single bleed nozzle per main engine, the mass flow for the BN-Sippel cycle will be combined and rescaled to create a single outflow condition in the following.

For the simulations of the RET-1S bleed nozzles, the same temperatures and exit velocities compared to the BN-Sippel cycle are desired. Therefore, the exit temperature and velocity are set to $T_{BN,e} = 230.15$ K and $u_{BN,e} = 2240.18$ m/s. These values can be used to calculate the exit Mach number of the bleed nozzles:

$$\mathrm{M}_{BN,e} = \frac{u_{BN,e}}{\sqrt{\gamma R T_{BN,e}}} = 1.94, \tag{3.3}$$

with $R = 4124$J/(kg K) and $\gamma = 1.41$. The values for the specific gas constant and heat capacity ratio were calculated with the *NASA CEA tool* [27].

In the next step, the rescaling of the exit conditions is done by calculating the ratio of mass flow rates for the corresponding main engines. In case of RET-1S the main engine mass flow equals $\dot{m}_{main,RET} = 315.81 kg/s$, while the mass flow for the BN-Sippel case is given by $\dot{m}_{main,ref} = 539.29$kg/s. This leads to a mass flow ratio of:

$$r_{\dot{m}} = \frac{\dot{m}_{main,RET}}{m_{main,ref}} = 0.59. \tag{3.4}$$

This ratio is multiplied with the combined mass flow of the two bleed nozzles, which is used to power the oxidizer and fuel pumps, resulting in:

$$\dot{m}_{BN,RET} = r_{\dot{m}} \cdot \dot{m}_{BN,ref} = 6.27 \ \frac{\mathrm{kg}}{\mathrm{s}}. \tag{3.5}$$

By comparing the mass flow of the main engine with the secondary nozzle exhaust per engine, it can be seen, that the secondary nozzle exhaust only makes up 1.99 % of the main engine exhaust.

With the following equation, the Mach number together with the exit pressure in the BN-Sippel case are used to calculate the total pressure in the combustion chamber:

$$P_c = P_e \cdot \left[\frac{\gamma - 1}{2} \cdot \mathrm{M}_e^2 + 1 \right]^{\frac{\gamma}{\gamma-1}} = 2.84 \text{ bar}. \tag{3.6}$$

The throat area for the previously defined RET-1S bleed nozzle, with the corresponding exit area of $A_e = 0.063$ m^2 and the resulting supersonic area ratio of

$r_{\text{sup}} = 1.62$ is calculated by:

$$A_t = A_e \cdot \text{M}_e \cdot \left[\frac{1 + \frac{\gamma-1}{2} \cdot \text{M}_e^2}{\frac{\gamma+1}{2}} \right]^{-\frac{\gamma+1}{2(\gamma-1)}} = 0.039 \text{ m}^2. \tag{3.7}$$

The density inside the combustion chamber is calculated from the ideal gas law:

$$\rho_c = \frac{P_c}{R \cdot T_c} = 0.17 \frac{\text{kg}}{\text{m}^3}, \tag{3.8}$$

where T_c is the total temperature in the combustion chamber given by:

$$T_c = T_e \cdot \left(1 + \frac{\gamma - 1}{2} \text{M}_e^2 \right) = 312.7 \text{ K}. \tag{3.9}$$

A table of the relevant combustion chamber parameters derived in this section is given in tab.(3.4). These parameters will be used to conduct separate 2D-axisymmetric nozzle simulations in sec. 3.2.4.

Table 3.4.: Calculated combustion chamber conditions for the bleed nozzle outflow in the separate 2D-axisymmetric nozzle simulations in sec. 3.2.4.

Properties	Units	RET-1S bleed nozzle
Pressure	bar	2.84
Temperature	K	312.7
Density	kg/m^3	0.17

3.2.3. Estimation of the gas generator chamber conditions

The gas generator cycle represents the alternative modelling approach for the secondary nozzle outflow. Due to the similar chamber conditions of the RET-1S main engines and the Vulcain engine, the engine parameters of the Vulcain gas generator are used as reference values. The cycle will be referred to as V-GG and the technical characteristics can be taken from the work of Brossel et al. [3].

The gas generator of the Vulcain main engine uses a fuel rich mixture of liquid hydrogen, liquid oxygen with an oxidizer to fuel ratio of $\frac{O}{F} = 0.9$. As already mentioned in sec. 2.1, this is done to keep the exhaust gas temperatures below the melting point of the turbine blades. The hot exhaust gas is then used to power the oxidizer and fuel pumps. A description of this process and the theory of an open

gas generator cycle was given in in the same section. For the sake of simplicity, the mass flow of the hydrogen turbopump is used for an estimation of all implemented pump-systems and for the inflow conditions of the secondary nozzle.

The hydrogen turbopump is characterized by a turbine inlet pressure of $P_\text{in} = 75$ bar and an inlet temperature of $T_\text{in} = 900$ K. The heat capacity ratio of $c_\text{p} = 8083.3\text{J}/(\text{kg K})$ for the species mixture is calculated with the *NASA CEA tool*. The turbine outlet temperature T_out can be estimated by subtracting the change in enthalpy, due to the turbine power generation of $P = 12$ MW and the mass flow of $\dot{m}_\text{GG,ref} = 9.2$ kg/s, from the inlet temperature:

$$T_\text{out} = T_\text{in} - \frac{\Delta h}{c_\text{p}} = 723 \text{ K}. \tag{3.10}$$

The chamber pressure can then be derived with the isentropic expression:

$$\left(\frac{\rho_\text{out}}{\rho_\text{in}}\right)^\gamma = \frac{P_\text{out}}{P_\text{in}} = \left(\frac{T_\text{out}}{T_\text{in}}\right)^{\frac{\gamma}{\gamma-1}} \Rightarrow P_\text{out} = 35.4 \text{ bar} \tag{3.11}$$

with a heat capacity ratio of $\gamma = 1.37$ for the exhaust gas mixture. The heat capacity ratio was taken from the output of the *NASA CEA tool*. The density can again be calculated with the ideal gas law (eq.(3.8)), leading to a value of $\rho_\text{out} = 2.26 \text{ kg/m}^2$.

Table 3.5.: Calculated combustion chamber conditions for the gas generator outflow in the separate 2D-axisymmetric nozzle simulations.

Properties	**Units**	**RET-1S gas generator**
Pressure	bar	3.32
Temperature	K	383.8
Density	kg/m³	0.4

These nozzle inlet conditions would lead to a significantly increased mass flow for the secondary nozzles in separate simulations (see sec. 3.2.4). Therefore, the chamber inflow density had to be adjusted with respect to the nozzle inflow diameter and the mass flow leading to a value of $\rho_\text{out} = 0.4 \text{ kg/m}^3$. The adjusted inlet pressure equals $P_\text{out} = 3.32$ bar.

3.2.4. Nozzle simulations and interpolation setup

In order to guarantee realistic conditions for the engine outflow and a high resolution of the boundary layer close to the nozzle walls in the 3D simulation setup of the RET-1S-vehicle, separate 2D-axisymmetric simulations of the nozzle flow are conducted. The derived chamber conditions of the bleed nozzle (sec. 3.2.2) and gas generator (sec. 3.2.3) in addition to the main engine combustion chamber conditions are used as inflow conditions. It was observed, that a high resolution of the nozzle shear layer improves the numerical accuracy of the 3D simulations and leads to a more accurate representation of the exhaust jet structure and plume length.

For the main engine, the gas burned in the combustion chamber consists of a mixture of liquid hydrogen and oxygen with the chamber conditions given in tab.(3.6), while the outlet pressure is defined by the vehicle altitude. Therefore, multiple simulations had to be done for the varying outlet pressures. Since the flow is assumed to be in chemical non-equilibrium, a reduced 19-step Jachimowski mechanism with 9 species is applied in all simulations. The result for the Mach number distribution is shown in fig.(3.3 a)).

Table 3.6.: Combustion chamber conditions of the RET-1S main engines.

Properties	Units	RET-1S main engine
Pressure	bar	117.3
O/F	–	6.7
Density	kg/m^3	5.44

(a)   (b)
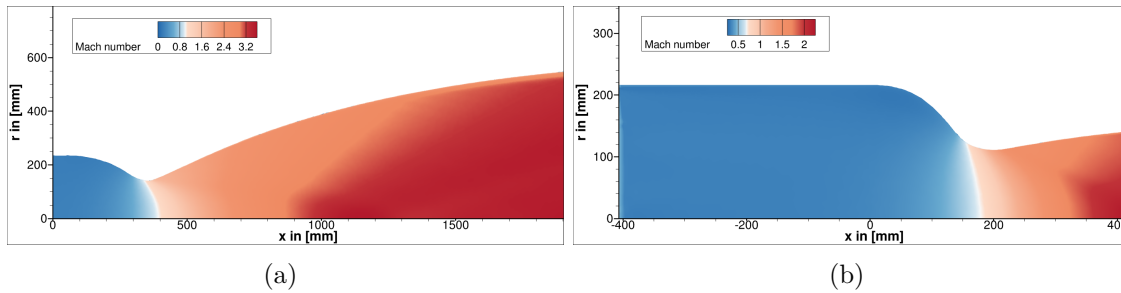
Figure 3.3.: a) Main engine Mach number distribution. b) Bleed nozzle Mach number distribution.

No nozzle contour was available for the secondary nozzles. Therefore a generic nozzle contour was created by using the predefined outlet area and the nozzle throat area derived in eq.(3.7), leading to the supersonic area ratio of $r_{\mathrm{sup}} = 1.62$. The nozzle contour was used for the simulations of the bleed engine outflow, as well as the gas generator conditions. Since the exhaust gas of the secondary nozzles in the bleed engine cycle only consists of hydrogen, the corresponding simulations were done for a single species transport with the chamber conditions given in tab.(3.4). The reduced Jachmimowski mechanism is applied for the simulation of the gas generator flow due to the presence of an oxidizer and fuel mixture, making additional combustion possible. The Mach number distribution for the secondary nozzle is visualized in fig.(3.3 b)). The visualization of the nozzle flow through the main engine and secondary nozzle show the formation of the shear layer along the outer wall. In both cases a weak shock, forming downstream of the throat, is present inside the nozzle and the exit velocities are still supersonic.

Linear interpolation is used to map the generated nozzle outflow profiles as Dirichlet condition onto the corresponding boundary cells of the 3D simulations for the RET-1S vehicle. In order to create a good approximation of the circular outflow, a so called *Euler step* was created at the nozzle outlet. This *Euler step* consists of a backwards facing step into the nozzle connecting the outer nozzle wall with the Dirichlet inlet through a slip wall boundary marker (see fig.(3.4)). The slip wall condition is used to avoid numerical problems and non-converging solutions, which occur for a boundary marker with a no-slip condition close to the supersonic inflow boundary marker due to the high gradients in flow velocity.

Without applying the *Euler step* and placing the supersonic outflow condition directly onto the nozzle walls, the outer grid points of the boundary marker are assigned with the boundary condition and value from the viscous wall. This leads to a zic-zac shaped outflow condition of the nozzle, similar to the schematic visualization shown in fig.(3.5 a)). By applying the *Euler step* and resolving the boundary layer along the included grid markers, the shape of the supersonic outflow is improved and nearly circular, apart from the obvious discretization errors, leading to the result in fig.(3.5 b)).
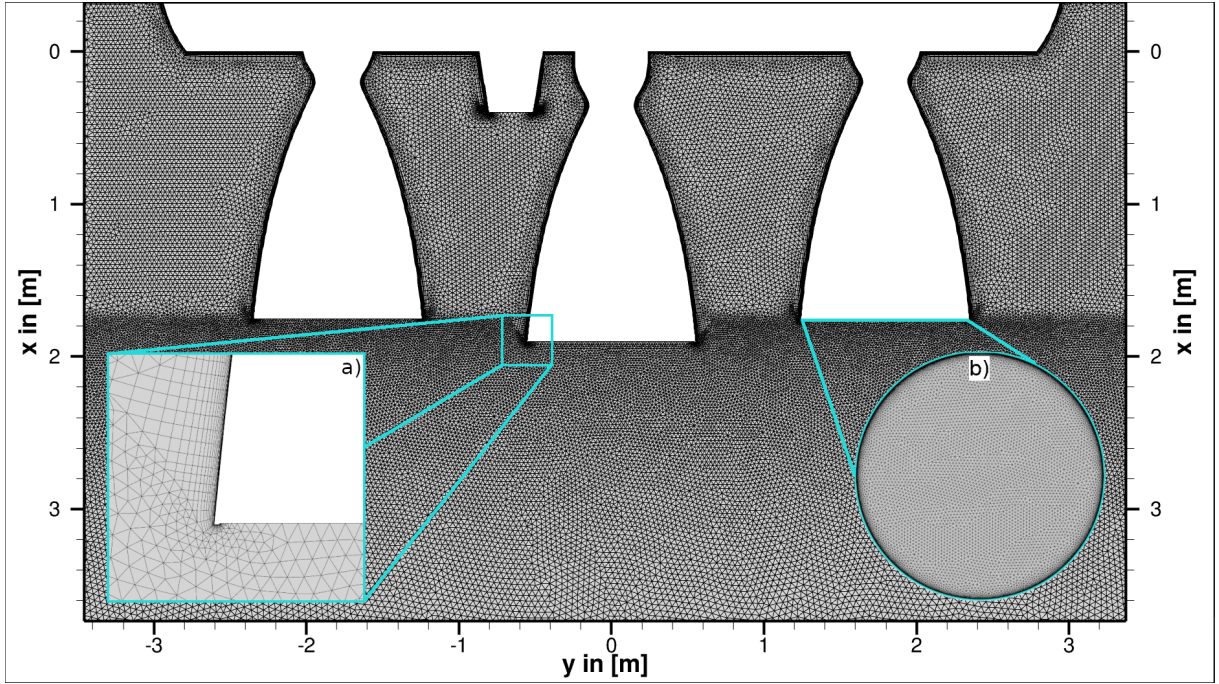
Figure 3.4.: Closeup of the aft-bay region of the RET-1S vehicle in the 3D simula-
tion mesh including a visualization of the *Euler step* and the Outflow
boundary marker of the main engines.

3.3. Grid convergence study

The quality of the numerical mesh is verified by conducting a grid convergence study
utilizing the Grid Convergence Index or short GCI-methodology proposed by Celik
et al.[5]. For this purpose, three different grids with varying cell size in the refinement
region of the exhaust plume are generated. The fine, medium and coarse grid consist
of $N_1 = 108$ M, $N_2 = 49$ M and $N_3 = 27$ M volume elements, respectively. The
first layer thickness of the numerical mesh is kept constant in order to guarantee
the dimensionless wall distance of $y^+ < 1.0$. As already mentioned in sec. 3.2.1 this
is required for simulations with one-equation Spalart-Allmaras turbulence models
without wall functions.

The first step of the GCI-study is to define a representative mean cell size for the
three meshes. Since the grid volume elements are given by tetrahedrons, the equation
for the cell size is given by:

$$h = \left[\frac{12}{\sqrt{2}N} \sum_{i=1}^{N} (\Delta V_i) \right]^{\frac{1}{3}},$$ (3.12)
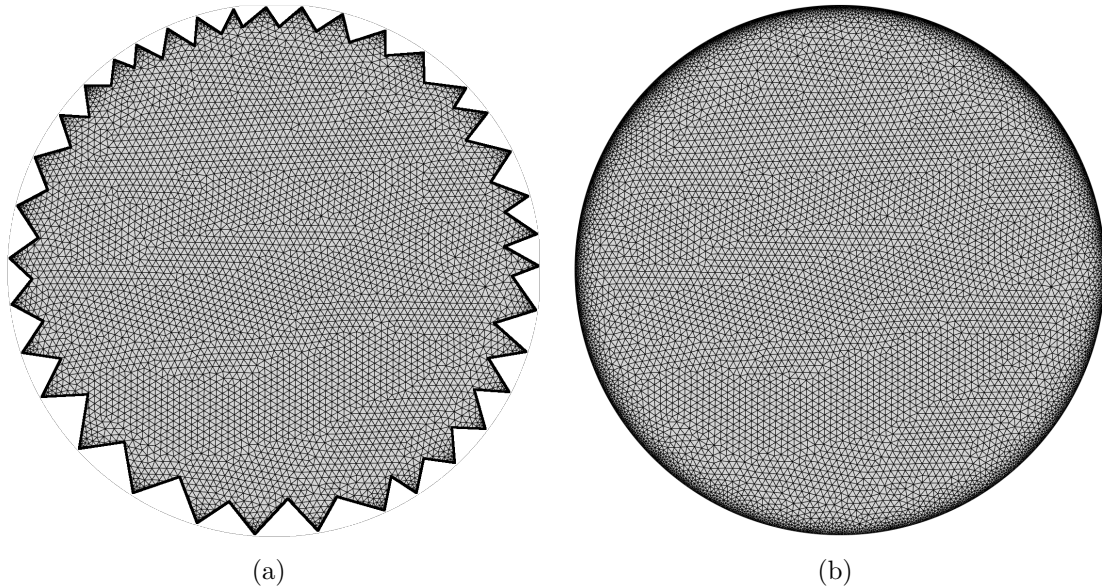
Figure 3.5.: a) Schematic representation of the nozzle inflow boundary marker without *Euler step* b) Visualization of the nozzle inflow boundary marker with implemented *Euler step*.

where h is the edge length of the tetrahedron, V_i is the volume of the ith cell and N is the total number of cells used for the computation and therefore dependent on the number of volume elements in the plume refinement region of the coarse, medium and fine mesh. The fine, medium and coarse cell size are characterized by $h_1 < h_2 < h_3$, which follows directly from the increasing cell size for a coarser resolution of the computational domain. A table containing the general edge length of the three meshes in the conical and cylindrical grid refinement region is given in Appendix B.

With these representative cell sizes, the refinement factors between the three different meshes defined as:

$$r_{\text{coarse,fine}} = \frac{h_{\text{coarse}}}{h_{\text{fine}}} \tag{3.13}$$

is calculated, leading to a value of $r_{21} = 1.36$ for the medium and fine mesh and $r_{32} = 1.33$ for the coarse and medium mesh. This is in range of the suggested value of $r > 1.3$. As stated in [5], the suggested value is based on experience. Smaller values lead to a non-converging behaviour and numerical problems during the calculation.

The GCI-methodology is derived from the Richardson extrapolation [33] and its ap-

parent order p is used in the calculation of the GCI. The apparent order is calculated by a fixed-point iteration using the following expressions [5]:

$$p = \frac{1}{\ln\left(r_{21}\right)} \left| \ln \left| \frac{\epsilon_{32}}{\epsilon_{21}} \right| + q(p) \right|, \tag{3.14}$$

$$q(p) = \ln \left(\frac{r_{21}^p - s}{r_{32}^p - s} \right), \tag{3.15}$$

$$s = 1 \cdot \text{sgn} \left(\frac{\epsilon_{32}}{\epsilon_{21}} \right), \tag{3.16}$$

with $\epsilon_{32} = \phi_3 - \phi_2$, $\epsilon_{21} = \phi_2 - \phi_1$ and ϕ_k being the solution of the flow variable used for the GCI calculation on the kth grid. The starting point of the fixed-point iteration is given by the first term of eq.(3.16a). Negative values for the quotient $\epsilon_{32}/\epsilon_{21}$ indicate oscillatory convergence of the numerical scheme. This oscillatory convergence can occur if one of the two epsilon values is close to zero, which can also mean, that the exact solution of the CFD problem is obtained. In this case the routine for the fixed-point iteration of the observed grid point does not work. The overall amount of oscillatory convergence is reported.

Together with the previously defined flow variable on two of the meshes, an extrapolated value can be calculated [5]:

$$\phi_{\text{ext}}^{21} = \frac{r_{21}^p \phi_1 - \phi_2}{r_{21}^p - 1} \tag{3.17}$$

which is then used in the calculation of the relative extrapolated error. This extrapolated error is defined as [5]:

$$e_{\text{ext}}^{21} = \left| \frac{\phi_{\text{ext}}^{21} - \phi_1}{\phi_{\text{ext}}^{21}} \right|. \tag{3.18}$$

In addition to the extrapolated error, the relative error is defined as [5]:

$$e_a^{21} = \left| \frac{\phi_1 - \phi_2}{\phi_1} \right|. \tag{3.19}$$

The approximated relative error, together with the refinement factor of the corresponding meshes and the apparent order of the Richardson extrapolation is used to

calculate the grid convergence index [5]:

$$\text{GCI}^{21}_{\text{fine}} = \frac{1.25 e^{21}_a}{r^p_{21} - 1}. \tag{3.20}$$

In the previous equations the fine-grid convergence index and the relative errors between the medium and fine mesh were defined, however the same relations hold for the coarse-grid convergence index and relative errors.

In the following the results of the GCI-study will be discussed. The representative flow variables chosen for the GCI-study are the temperature and Mach number in case of the flow field solution and the heat flux along the baseplate for the surface values. The resulting numerical errors are given in tab.(3.7).

Table 3.7.: GCI Results and relative errors of the integrated heat flux.

mean error in %	Mach-Field	Temp.-Field	Baseplate heat flux
GCI errors			
e^{21}_a	1.62	1.24	12.27
e^{21}_{ext}	0.83	0.67	3.52
$\text{GCI}^{21}_{\text{fine}}$	1.01	0.84	4.39
e^{32}_a	1.29	0.80	5.06
e^{32}_{ext}	0.95	0.56	3.51
$\text{GCI}^{32}_{\text{coarse}}$	1.16	0.70	4.05
oscillatory conv.	25.70	83.55	46.85
apparent order p	16.11	14.19	13.25
relative errors interpolated heat flux			
$e_{\text{fine/medium}}$	−	−	2.15
$e_{\text{med/coarse}}$	−	−	1.30

† superscript ^{21}: error medium-fine mesh; superscript ^{32}: error coarse-medium mesh

The small relative errors and GCI-values of the field variables, in addition to the high amount of oscillatory convergence concerning the temperature field, indicate that the results on the different meshes are in good agreement. This can be verified by comparing the flow field and profile lines of the Mach number and temperature in fig.(3.6), showing that the overall characteristics remain the same, while the shock distance and intensities are slightly underestimated for coarser meshes due to the high resolution needed in these areas.

Concering the heat flux distribution along the baseplate, high relative errors in range

of 12.27% and 5.06% were observed for the fine- and coarse grid error, respectively. The reason for these high values is that the GCI-methodology uses a pointwise comparison of the characteristic values along the grid nodes, neglecting high gradients of the variables common to supersonic flow. In order to estimate an error independent of the local spacing and preserving the gradients in the heat flux distribution, the relative error of the integrated heat flux is calculated for the three meshes, leading to values of 2.15% for fine mesh error and 1.3% for the coarse mesh error. The corresponding plot of the heat flux distribution along the baseplate is given in fig.(3.7). These results lead to the conclusion that the solution on the numerical meshes is converged. This indicates that the resolution on the medium mesh is sufficient for our purpose and is able to capture the occurring flow characteristics and heat flux distributions in the aft-bay region of the vehicle. Therefore the medium mesh is used in all subsequent simulations [15].
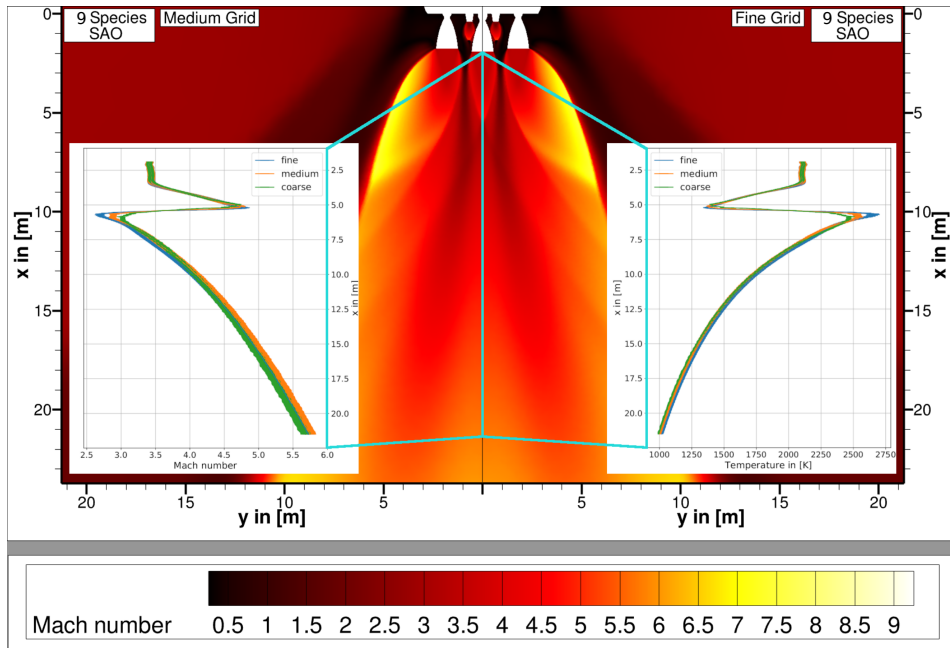
Figure 3.6.: Comparison of the flow fields for the solution on the medium and fine mesh, including the temperature and Mach number profile along the center line. The simulations were done using a 9 species, reacting chemistry mixture and the Spalart-Allmaras (SAO) turbulence model.
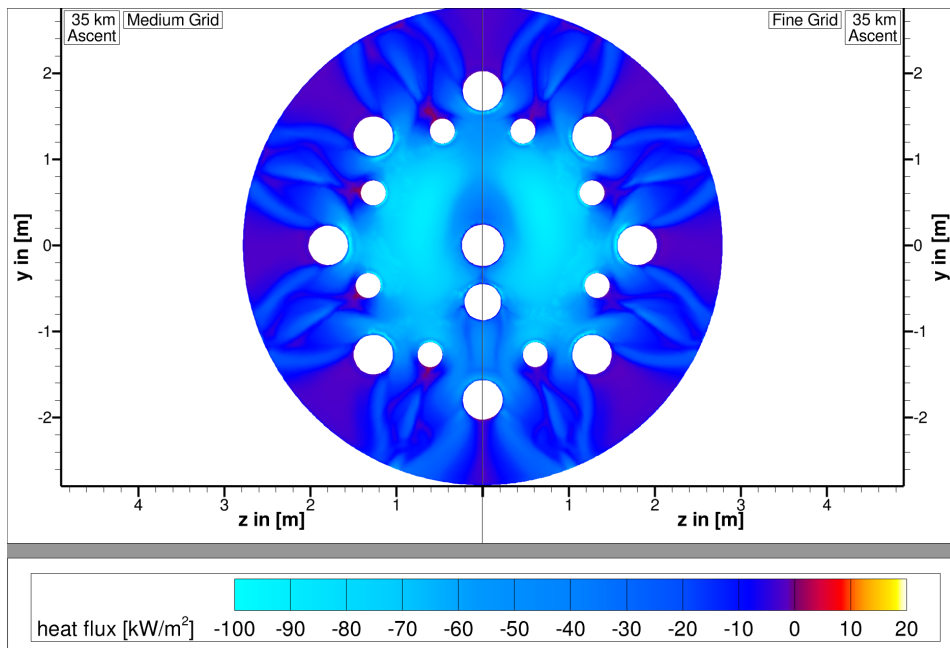

Figure 3.7.: Comparison of the heat flux distribution along the baseplate of the RET-1S-vehicle for the solution on the medium (left) and fine mesh (right).

4. Results

The results of the 3D CFD simulations for the RET-1S vehicle will be discussed in this section to give an assessment of the heat flux and to describe the observed characteristics along the baseplate. The simulations include trajectory points during the ascent phase from an altitude of 7 km up to 86 km and during the retro-burn phase. An overview of the trajectory points and boundary conditions is given in tab.(3.1).

During these flight phases the flowfield in the aft-bay region is dominated by the main engine and secondary nozzle exhaust plume structure. For the ascent phase all of the first stage engines are active, leading to an outflow of exhaust gas from $N_1 = 3 + \frac{3}{2}$ of the main engines and $N_2 = 4 + \frac{1}{2}$ of the bleed nozzles in the half model. A visualization of the half model baseplate and openings for the engines is given in fig.(4.1). The main engine and secondary nozzle openings are colored in turquoise and red respectively. Due to the elevation and conical shape of the central
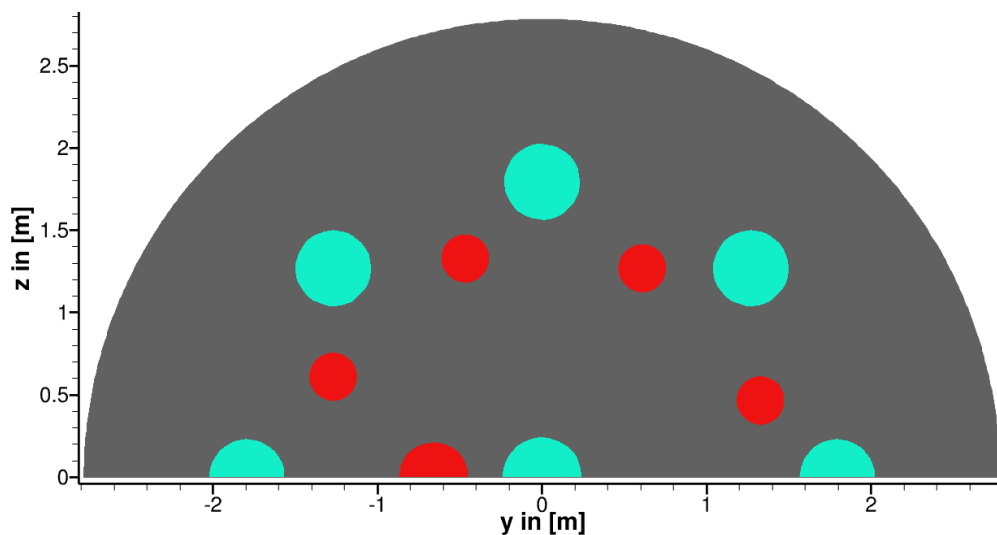

Figure 4.1.: Visualization of the baseplate openings for the half model with $N_1 = 3 + \frac{3}{2}$ main engines colored in turquoise and $N_2 = 4 + \frac{1}{2}$ secondary nozzles colored in red.

secondary nozzle the diameter of the baseplate opening is projected slightly larger in the baseplate-plane.

For the retro-burn phase only the 3 central main engines along the y-z-plane and the corresponding bleed nozzles are active, which will be marked in the flowfield and baseplate plots. The simulations for the retro-burn phase are done for the 360° full model of the vehicle.

In the first step, the overall influence of the secondary nozzles is analyzed by comparing simulation results for activated and deactivated bleed nozzles during the ascent and retro-burn phase for an altitude of 35 km and 40 km, respectively. Afterwards the heat flux characteristics for the expander bleed engine cylce are compared to the gas generator cycle. Finally the flowfield and heat flux characteristics during the ascent and retro-burn phase will be discussed for the observed trajectory points.

4.1. The influence of the additional bleed nozzle outflow during the ascent phase

In this section the influence of the bleed nozzle outflow will be analyzed by comparing the results with a configuration in which the bleed nozzles are deactivated. The simulations were done for an altitude of 35 km. The flowfields for the two configurations are shown in fig. 4.2, while the corresponding heat flux distritubions along the baseplate are given in fig. 4.3.

In fig. 4.2, the Mach number in the symmetry plane together with an iso-surface of negative axial velocities of $u = -200$ m/s is plotted for the configuration without bleed nozzle outflow on the left side and with active bleed nozzles on the right side. In order to give an estimation of the temperature distribution of the recirculating gas, the temperature color map is projected onto the iso-surface. The flowfield at an altitude of 35 km is characterized by highly underexpanded jets leading to a large spatial extension and strong plume-plume interactions. In general, the shock characteristics and flowfield structure downstream of the main engine exhaust remain similar in both cases, since the overall mass flow of the bleed nozzles adds only about 2% of the main engine exhaust.

In contrast to the downstream region, the additional outflow from the bleed nozzles has a strong effect on the flow structure in the aft-bay region and the cavities between the main engines. For deactivated bleed nozzles, a strong recirculation region forms around the central main engine and the gaps between the annular main en-

gines, which leads to the entrainment of hot exhaust gas towards the baseplate of the vehicle. This observation is in agreement with the heat flux distribution, which is shown in fig. 4.3 on the left. For a given wall temperature of 600 K, high thermal loads with local maxima in the range of $180 - 260$ kW/m^2 can be identified between the central nozzle and the outer ring of nozzles in addition to the gaps between them. The maxima are located in front of the nozzle-baseplate intersections of the main engines in positive radial direction. The nozzles themselves have a shielding effect on the baseplate region behind them, where the heat flux is moderately low, up to 20 kW/m^2. This simulation setup of the reduced RET-1S-vehicle leads to comparable results with the RETALT1 database derived by Laureti et al.[23] and the same flow field characteristics are observed.

For active bleed nozzles, a significant change in the flowfield and the base heating can be identified. Due to the additional outflow of cold hydrogen with an average temperature of $T_e = 230.15$ K, velocity of $v_e = 2240.18$ m/s and Mach number of $M = 1.94$, the recirculation and entrainment of hot exhaust from the main engines is prevented in most areas, as shown by the iso-surface of the negative velocities in fig. 4.2. The bleed nozzle exhaust jets lead to a constriction of the main engine exhaust in the area around the nozzles, which can be seen in the Mach number distribution. The main recirculation region can be identified around the central nozzle further outward of the central or annular bleed nozzles. In contrast to the configuration without bleed nozzle outflow, the temperature of the recirculating gas, which is mainly composed of the bleed nozzle outflow or main engine exhaust cooled by it, is significantly reduced and the highest values can be found around the central main engine outlet again. By comparing these results with the heat flux distribution in fig. 4.3 on the right side, we observe that the cold hydrogen leads to a significant reduction of the heat flux values in range of [-100;20]kW/m^2. The minima are found in the central region close to the bleed nozzles and along the edges of the outer main engines. The cold gas outflow only has a small influence on the heat flux values behind the baseplate openings of the main engines in the peripheral region of the baseplate. [15]

The mean heat flux during the ascent phase for the configuration with active and deactivated bleed nozzles is given by $\bar{q}_{\text{BN on, ASC}} = -18.9$ kW/m^2 and $\bar{q}_{\text{BN off, ASC}} = 48.2$ kW/m^2, respectively. A significant reduction of the thermal loads and a negative mean heat flux for the configuration with active bleed nozzles is

observed for a wall temperature of 600 K. This observation leads to the conclusion, that the additional secondary nozzle outflow has a positive influence on the aerothermal loads during the ascent phase of the launch vehicle and protects the baseplate against the hot main engine exhaust.

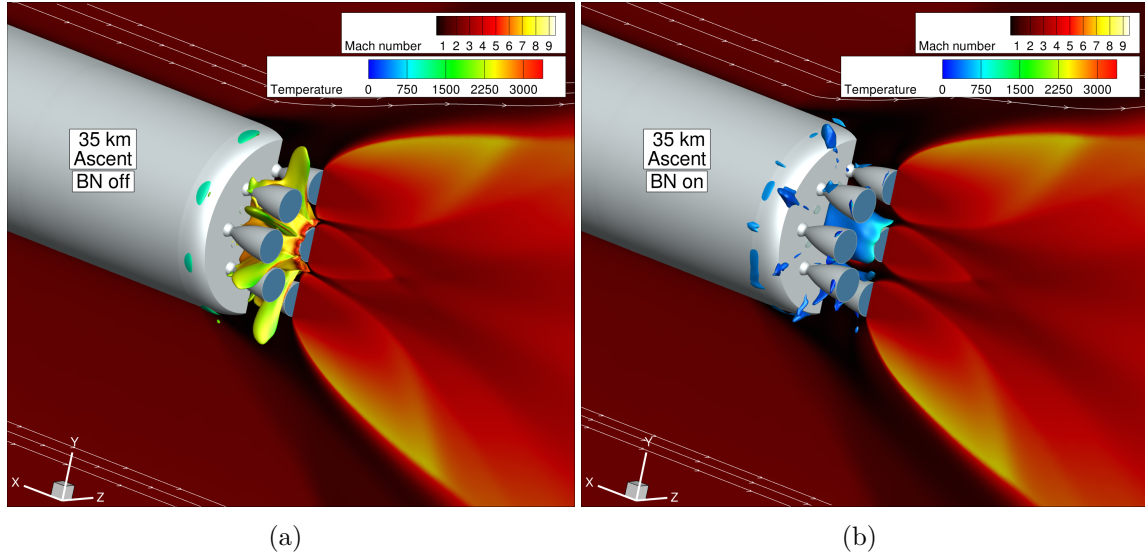(a)   (b)

Figure 4.2.: Flowfield represented by the Mach number and iso-surface with negative axial velocity of $u = -200$ m/s for a) the configuration with deactivated bleed nozzles and b) the configuration with active bleed nozzles.
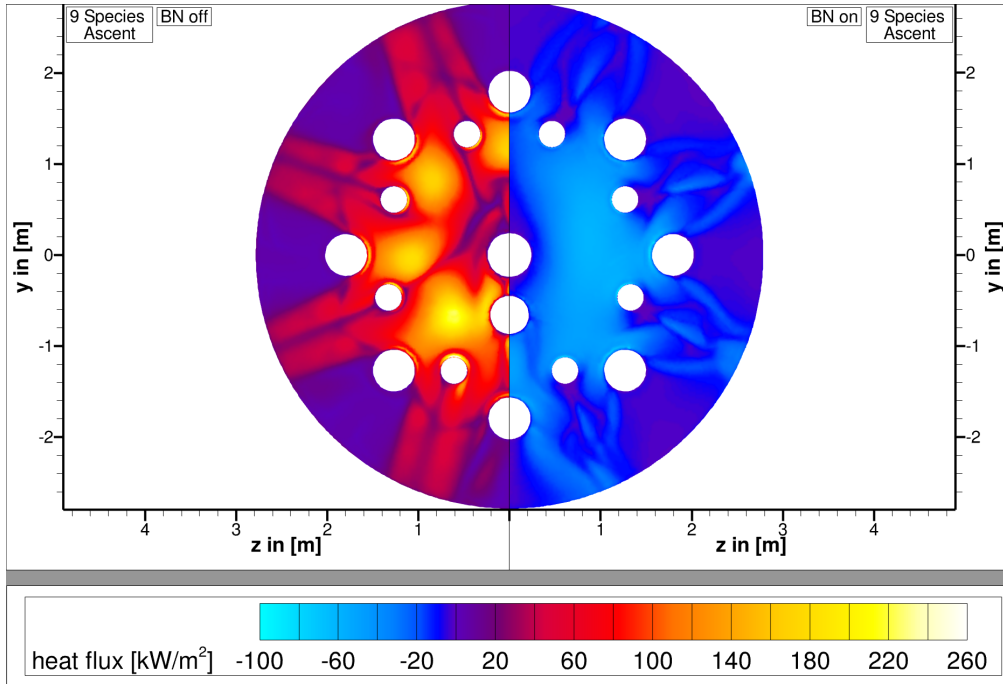
Figure 4.3.: Comparison of the heat flux distribution along the baseplate for an altitude of 35 km along the ascent trajectory. Left side: bleed nozzles off, right side: bleed nozzles on.

4.2. The influence of the additional bleed nozzle outflow during the descent phase

As in the previous section, the influence of the additional bleed nozzle outflow on the flowfield characteristics and the heat flux distribution along the baseplate of the RET-1S vehicle will be discussed for the retro-burn phase by comparing the numerical results for simulations with activated and deactivated secondary nozzles. The simulations were done for an altitude of 40 km, corresponding to the second descent trajectory point in tab.(3.1). The heat flux distribution along the baseplate is shown in fig.(4.4). During the retro-propulsion phase the engines are operated towards the free stream flow direction. Additionally, only 3 of the main engines are active, and in case of active secondary nozzles the corresponding bleed engines. This leads to an increasing complexity of the flow field and the occurrence of strong non-symmetric recirculation regions. Therefore a single field cut through the symmetry plane is not sufficient to capture all relevant flow characteristics. The position of the field cuts is indicated by the black lines along the baseplate of the vehicle in fig.(4.4), while the field cuts themselves are given in fig.(4.5, 4.6). The active engines are indicated by a

green coloration of the baseplate openings in the heat flux plot and the temperature color map in the field plot.
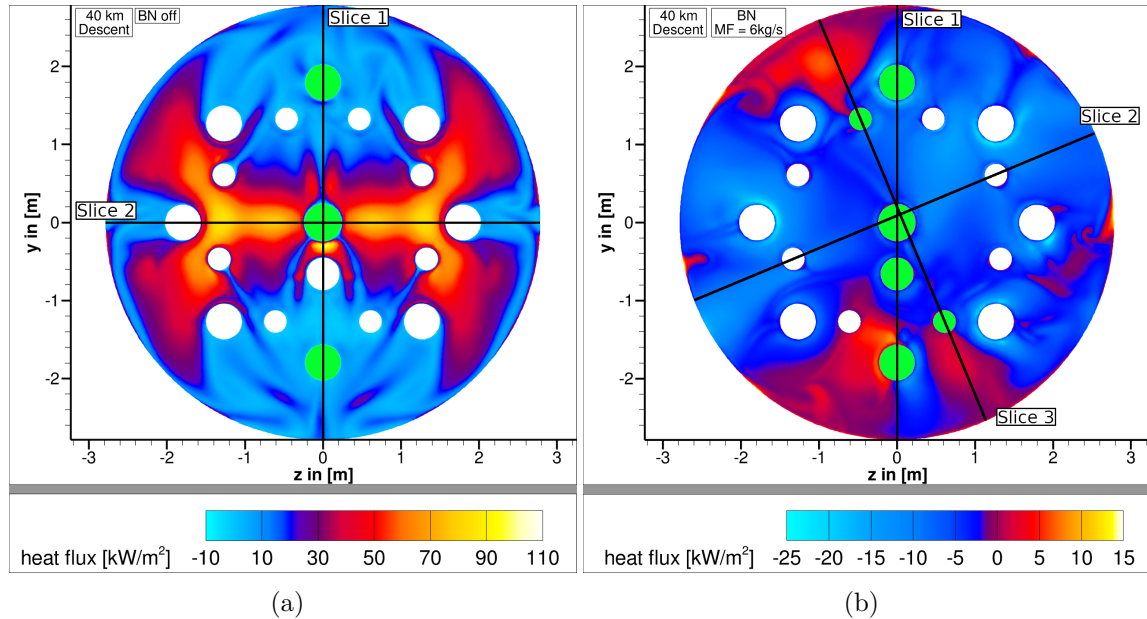

Figure 4.4.: Baseplate heat flux distribution for the descent configurations at an altitude of 40 km. In both figures, the indication of the field cuts used for the visualization of the flow fields is given by the black lines and the corresponding name tags. Additionally the active main and bleed engines are marked by a green coloration of the baseplate opening. (a) Configuration with deactivated bleed nozzles. (b) Configuration with active bleed nozzles.

A visualization of the flow field with deactivated secondary nozzles is given in fig.(4.5). The Mach number in the corresponding slice is plotted in gray scale, while the 3D streamlines and rocket body are colored with the temperature color map.

For the altitude of 40 km, the relatively low atmospheric pressure leads to a highly underexpanded configuration of the supersonic exhaust jets and strong plume-plume interactions can be observed. The flowfield downstream of the main engines is again similar for the two cases with active and deactivated secondary nozzles. Expansion fans form at the nozzle exits of the main engines, which are reflected at the outer shear layer of the supersonic exhaust jets and lead to the formation of a barrel shock downstream of the main engines. The barrel shock ends in a Mach disk. The

counterflowing jets lead to the formation of a bow shock between the main engine exhaust and the incoming free stream flow, creating a stagnation region separating the vehicle from the incoming flow. This phenomenom is similar to the flowfield of a blunt body during retro-propulsion [10]. The theory behind it was described in sec. 2.4.2. In the aforementioned section, a visualization of the theoretical flow field regions and shock characteristics is included in fig.(2.6), which is in good agreement with the observed flow characteristics in this case fig.(4.5 a)).

Due to the interaction of the fluid passing through the bow and barrel shock, flow deflection of the hot main engine exhaust towards the vehicle occurs in the stagnation region. This leads to the immersion of the vehicle in the high temperature exhaust plume. The streamlines indicate the formation of a large torus-shaped recirculation area surrounding the aft-bay region. The highly underexpanded exhaust jets have a shielding effect on the baseplate, preventing the impingement of the free stream flow and leading to a shift of the recirculation region to a position further downstream of the aft-bay in the plane with operating main engines (x-y-plane). This shift is not observed in the perpendicular plane, where only the central main engine is active (Slice 2). Instead, the recirculation region is present in close proximity to the aft-bay. Additionally, due to the absence of the bleed nozzle outflow and the interaction of the exhaust jets directly at the nozzle outlets, an updraft plume forms. This updraft plume, which was described in sec.(2.4), leads to the entrainment of the main engine exhaust towards the baseplate and the formation of recirculation regions in the plane of active main engines. High flow velocities and therefore smaller temperatures are observed in close proximity to the wall, leading to the overall smaller heat flux values in the plane of active main engines. The flow in the recirculation regions impinges onto the nozzle walls and is deflected in perpendicular direction. Eventually, the recirculating fluid leaves the main engine cavities and aft-bay region in the same direction. A plot of the described flow characteristics can be seen in fig.(4.5 c)). This behaviour can also be seen in the base heat flux distribution. The overall heat flux values are in the interval of [-10;110] kW/m^2, leading to a mean heat flux of $\overline{q}_{\text{BN off, DEC}} = 20.9$ kW/m^2. In case of deactivated bleed nozzles, the same flowfield and heat flux characteristics compared to the aerothermal database can be observed [23].

Similar to the results in the previous section, the additional bleed nozzle outflow leads to a significant change in the flowfield and base heating in close proximity to
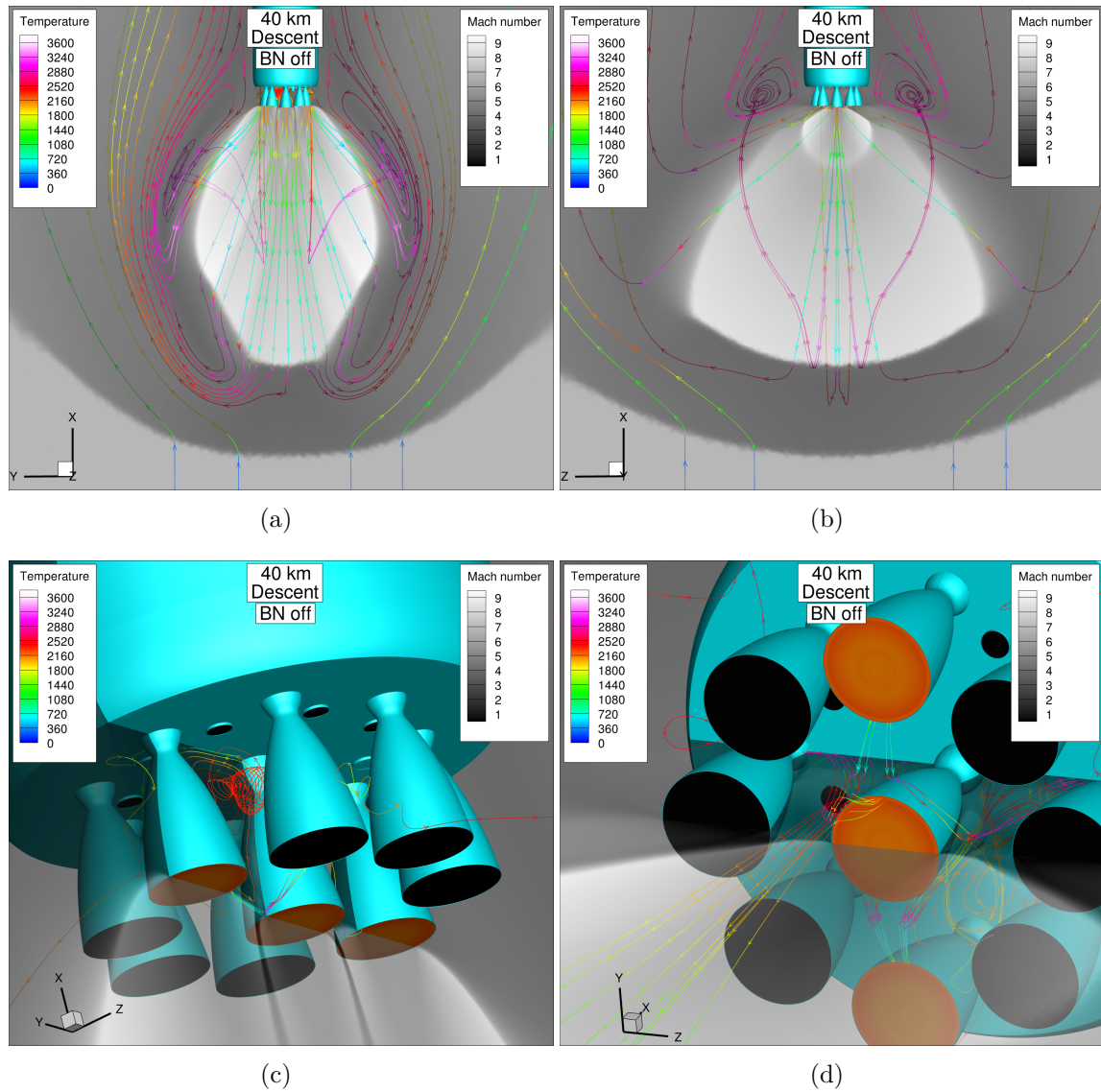
Figure 4.5.: Flowfield visualization for the simulated case with deactivated bleed nozzles. The Mach number distribution is plotted for the corresponding Slice in gray-scale and the streamlines are colored with the temperature color map. (a) Slice 1 through the active main engines and x-z-plane at the position y=0. (b) Slice 2 perpendicular to Slice 1 along the x-y-plane with z=0. A side view visualization of the two plots can be seen in Appendix C. (c) Closeup of the recirculation region in the plane of active main engines. (d) Closeup of the impingement and stagnation region of the hot main engine exhaust in the plane of deactivated main engines.

the aft-bay, while the overall exhaust plume structure remains approximately the same. The secondary nozzle exhaust jets prevent the backflow and recirculation of the hot main engine exhaust close to the nozzle outlets in the x-y-plane. By observing the flowfield in the plane of active bleed nozzles (Slice 3, fig.(4.6) d)), it can be seen that the bleed nozzle outflow leads to a constriction of the highly under-expanded main engine exhaust jets in radial outwards direction. This phenomenon locally reduces the shielding effect of the exhaust plume in close proximity to the secondary nozzle outlets compared to simulations with deactivated bleed nozzles. The baseplate close-up in fig.(4.6 d)) shows that a part of the hot main engine exhaust deflected by the incoming free stream and recirculating in the torus-shaped vortex ring is entrained towards the cavities of the main engines causing the hot spots in the heat flux distribution visualized in fig.(4.4 b)).

In the perpendicular plane with deactivated secondary nozzles (Slice 2, fig.(4.6) c)), the thermal loads and heat flux values are significantly reduced for a wall temperature of 600 K. This behaviour can be explained from the observation, that the inner portion of the bleed nozzle outflow in radial direction towards the coordinate origin impinges onto the main engine walls and is deflected. A visualization of this phenomenon is given in the close-up of the aft-bay region in fig.(4.6 c)). The deflected, high velocity bleed nozzle exhaust is directed in radially outwards direction and leaves the main engine cavities in the plane of deactivated secondary nozzles, preventing the entrainment of the main engine exhaust. The overall heat flux values in case of active bleed nozzles are in range of [-25; 15] kW/m², which corresponds to a mean heat flux of $\overline{q}_{\text{BN on, DEC}} = -2.8$ kW/m². Due to the weak constriction of the main engine exhaust by the secondary nozzle outflow, only a small amount of the hot main engine exhaust is entrained in the peripheral region of the baseplate. Therefore, even though local hot spots in the heat flux distribution are observed, the overall thermal loads for activated secondary nozzles are reduced compared to simulations with deactivated secondary nozzles.
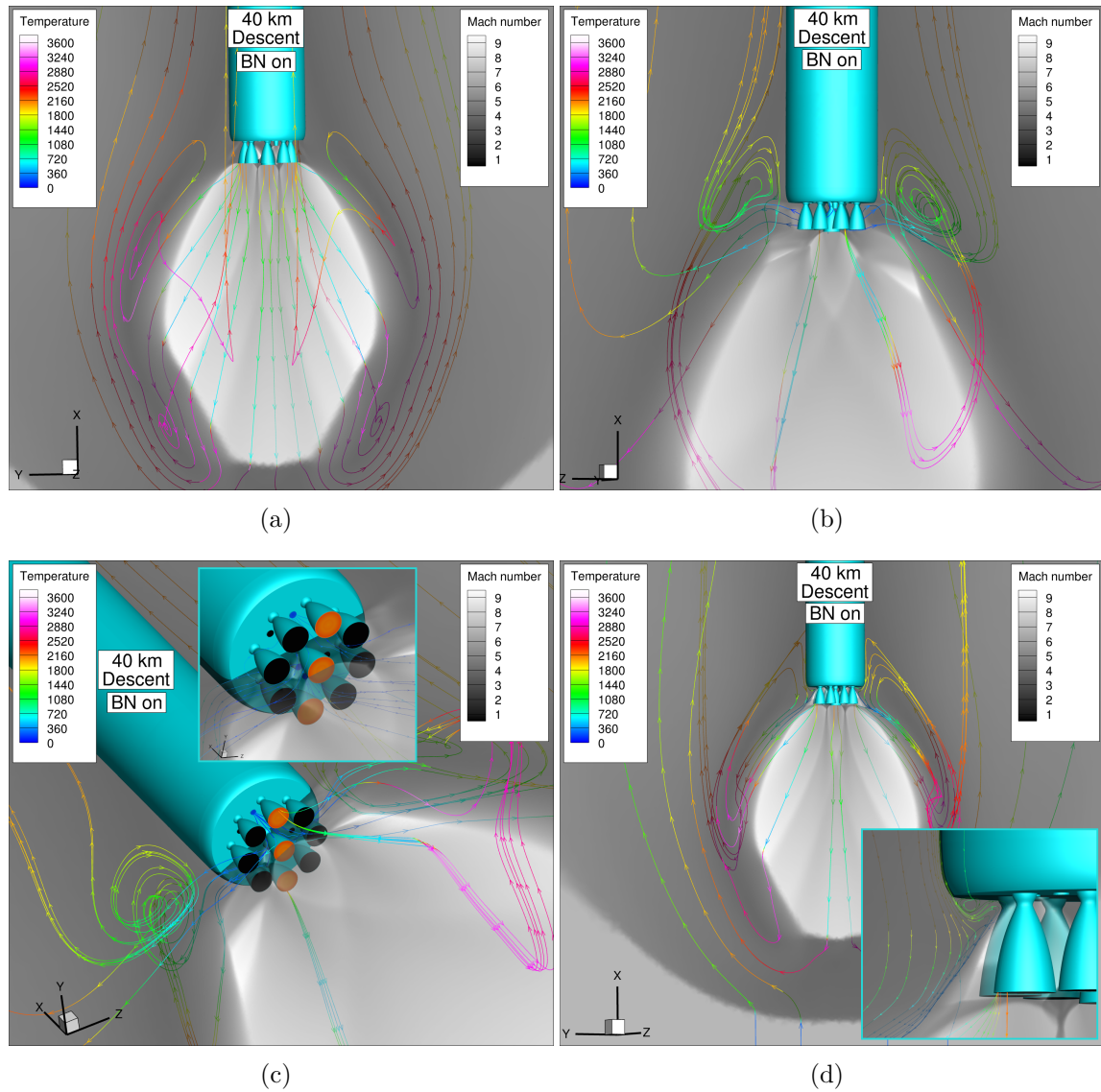
Figure 4.6.: Flowfield visualization for the simulated case with active bleed nozzles. The Mach number distribution is plotted for the corresponding Slice in gray-scale and the streamlines are colored with the temperature color map. Active main and bleed engines are indicated by the blue and orange outflow marker, representing the outlet temperature. (a) Slice 1 through the active main engines and x-y-plane at the position z=0. (b) Slice 2. (c) Slice 2 with a closeup visualization for the flow in the aft-bay region. (d) Slice 3 with a closeup visualization of the recirculation of the hot main engine exhaust towards the baseplate due to the constriction of the main engine exhaust jet by the bleed nozzle jet.

4.3. Comparision of the bleed nozzle and gas generator cycle

Two distinct simulations for the bleed engine and gas generator cylce for an altitude of 35 km along the ascent trajectory were done using the interpolated nozzle outflow profiles calculated with the chamber conditions derived in sec. 3.2.2 and sec. 3.2.3. The resulting heat flux distributions along the baseplate are shown in fig. 4.7.

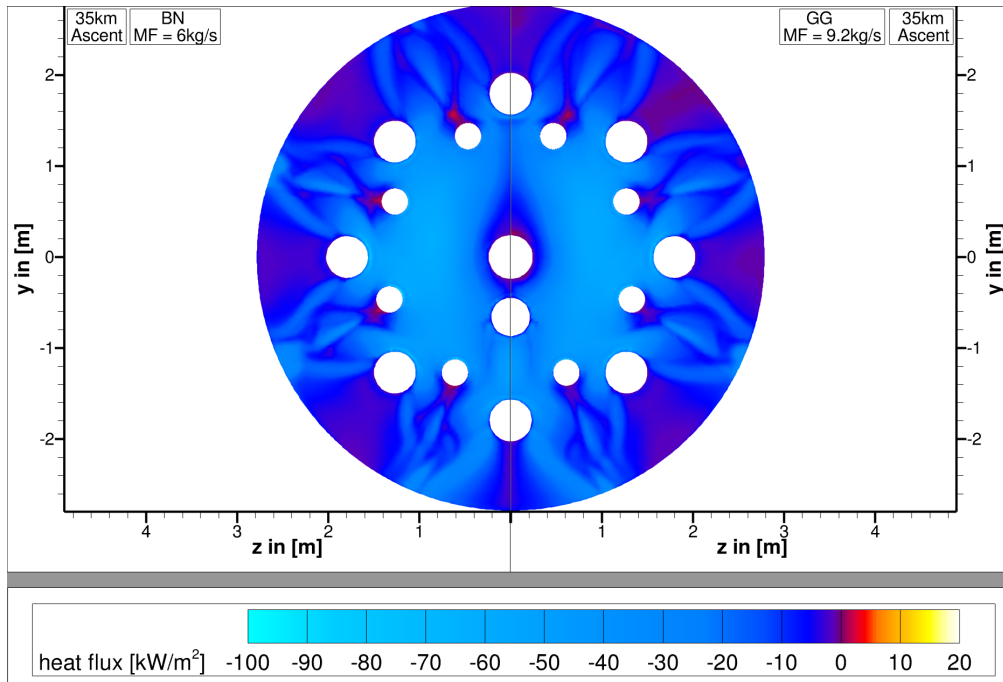Although the two engine configurations are characterized by slightly varying mass

Figure 4.7.: Comparison of the heat flux distribution along the baseplate of the RET-1S-vehicle for the bleed nozzle cycle, with pure hydrogen exhaust and gas generator cycle, with an exhaust mixture of water and hydrogen at slightly higher temperatures.

flows, species mixtures and thermodynamic states, the numerical results only show minor differences in the flowfield structure and heat flux distribution. It was proposed, that due to the fuel rich outflow of the secondary nozzles near the hot main engine exhaust, additional combustion with the ambient oxygen might occur. The distribution of the H_2-, O_2- and H_2O-mass fraction in the symmetry plane for the bleed engine cycle are given in fig.(4.8, 4.9). It can be seen that the species mixture in the main engine cavities mostly consists of unburned hydrogen and that some oxygen is entrained in the peripheral region of the baseplate. However, due to the

low temperature of the exhaust gas and the low densities of the ambient air, no post-combustion is observed and only a small amount of the hot main engine exhaust is entrained around the central main engine, where no secondary nozzles are present. Additionally, it was proposed that the changed species mixture of the gas generator cycle and higher total temperatures might lead to conditions, where additional combustion could occur. This is not the case and no post-combustion was observed. Therefore, varying the species mixture has no relevant influence on the heat flux distribution. The outlet temperature is approximately the same in both cases and the overall heat flux values remain in the range of [-100; 20] kW/m^2. Only a small increase in local heat flux can be seen for the gas generator configuration around the central main engine, while the spatial extend of the high heat flux region is reduced, and inside the wake area of the bleed nozzles close to the baseplate edge.

This observation leads to the conclusion that the simpler inflow condition of the bleed engine cycle is sufficient for our study and is therefore used in all subsequent simulations.
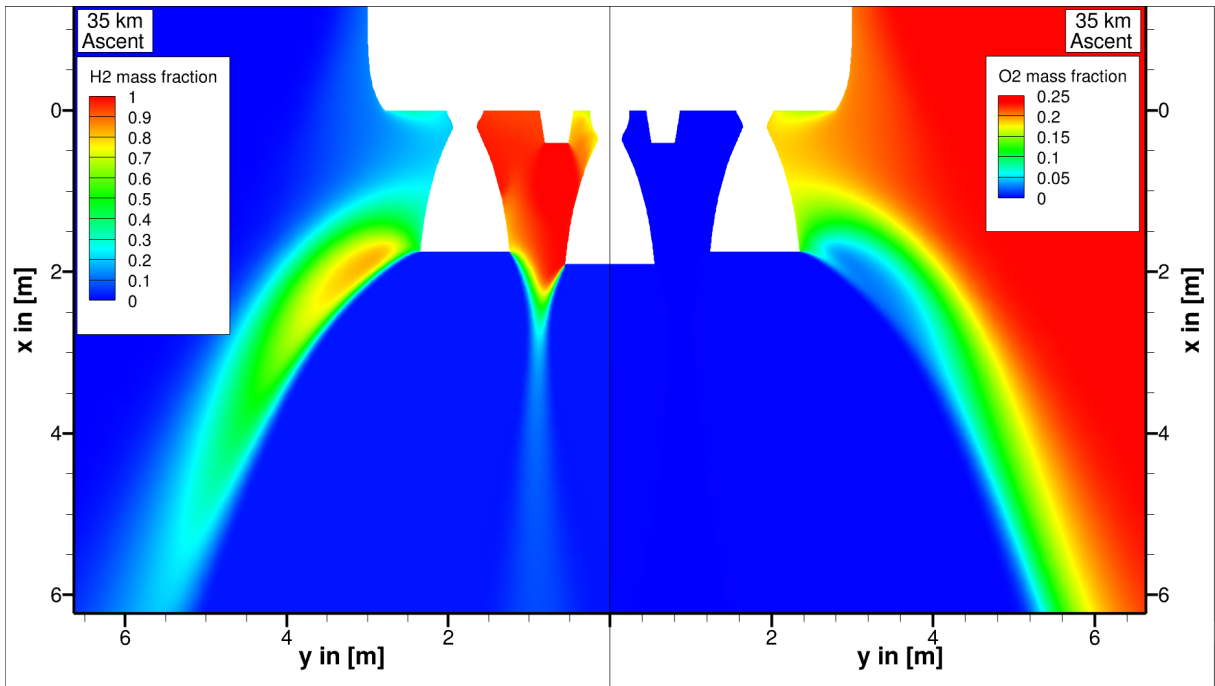
Figure 4.8.: H_2 and O_2 species mass fractions in the aft-bay region for the bleed engine cycle.
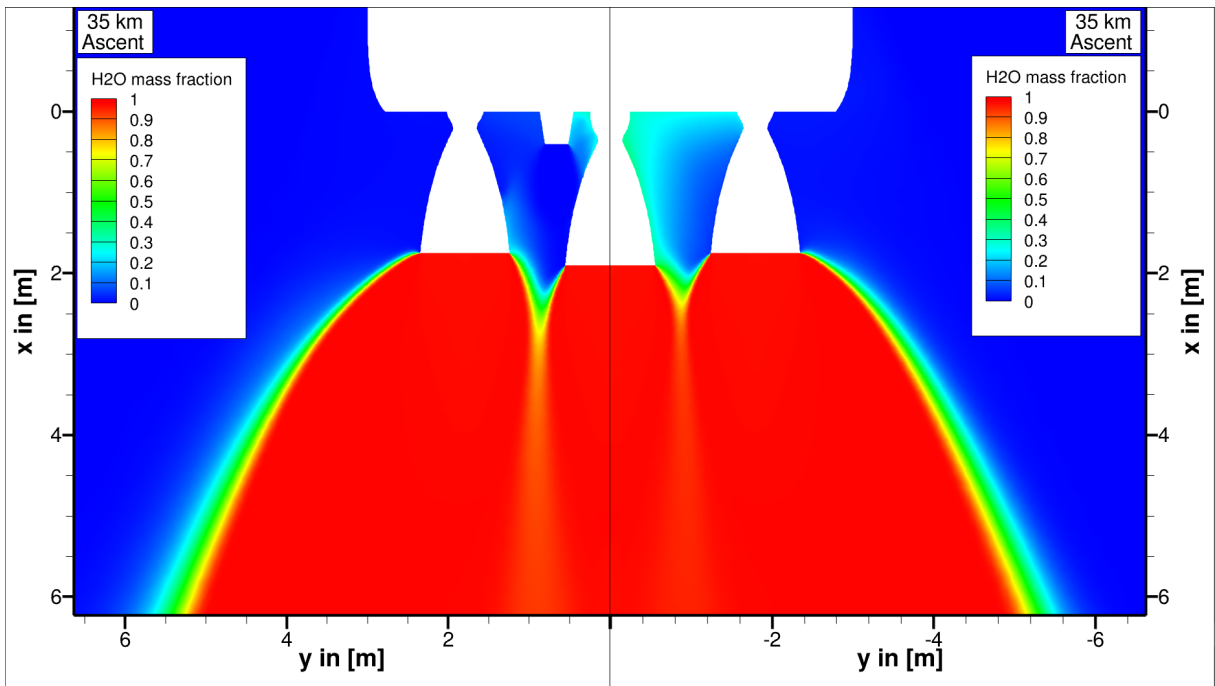

Figure 4.9.: H_2O species mass fraction in the aft-bay region for the bleed engine cycle.

4.4. Flowfield and thermal loads during the ascent trajectory

This section discusses the thermal loads on the baseplate for the ascent trajectory. During this phase the varying ambient pressure and flight Mach number lead to a wide range of flow regimes and different characteristics of the exhaust plumes. Representative flowfield visualizations are given in fig. 4.10. As in fig. 4.2, these plots show the Mach number along the symmetry plane and an iso-surface of negative axial velocity.

For altitudes lower than 7 km the large atmospheric ambient pressure leads to a confined structure of the supersonic exhaust jets, while the vehicle flight speed is still in the subsonic regime. Only weak plume-plume interactions are observed in close proximity to the main engine outlets, which increases along the downstream direction. In this case, only weak recirculation and backflow towards the baseplate occures. In order to visualize these regions, the negative axial velocity of the iso-surface was set to $u = -25$ m/s, while it was kept at $u = -200$ m/s for the configurations at higher altitudes. The temperature map, which differs from the one used in sec. 4.1, is projected onto the iso-surface.

It can be seen that the slow, recirculating gas in the peripheral region of the aft-bay exhibits temperatures in the range of the bleed nozzle outlet values. It is observed that due to the impingement of the secondary exhaust jets onto the outer nozzle walls of the main engines flow deflection occures leading to the entrainment of cold hydrogen. The results for the 7 km case were characterized by an unsteady, fluctuating behaviour of the flow along the baseplate, while the overall heat loads remained similar. The heat flux distribution can be seen in fig. 4.11 on the left, showing overall negative values in the range of [-100; -80] kW/m². In the area of the central main engine outlet, a slight increase in temperature was observed due to the interaction of the cold hydrogen gas with the exhaust plume.

For increasing altitudes the flow conditions in the aft-bay region become more stable. The main engine exhaust, which tends to form updraft plumes at the jet intersections, interacts with the additional hydrogen gas from the bleed nozzles and starts to enclose the baseplate region. Due to the higher underexpansion ratio for increasing altitudes, the base area surrounded by the exhaust plumes grows, while the exhaust jet structures in the central region remains the same. This effect leads to similar heat flux distributions in the central baseplate region for the 35 km (fig. 4.11) and

60 km (fig. 4.12) case while the peripheral region shows different characteristics. Above 60 km, the recirculating flow in the base region, which is enclosed by the highly underexpanded main engine exhaust jets, is separated from the free stream by a shear layer and the heat flux distribution along the baseplate remains the same. A plot comparing the baseplate heat flux for an altitude of 60 km and 86 km is given in fig. 4.12. Due to the increasing influence of the main engine exhaust, the heat flux in the peripheral aft-bay region increases since there are no bleed nozzles present to prevent the backflow. The heat flux values for higher altitudes are in the range of [-100;10] kW/m^2. The average base heat flux values for the simulated trajectory points are given in tab.(4.1).

The results can be divided in two major flow regimes, the low and high altitude configuration. While the low altitude simulations for heights below 7 km show confined plumes, weak recirculation and fluctuating heat fluxes on the baseplate, the high altitude configurations in the range of [35;86] km are characterized by stable flow conditions with highly underexpanded exhaust jets and strong plume-plume interaction.

The heat flux distribution is dominated by the exhaust plume structure of the main engines and bleed nozzles and converges towards a constant mean heat flux of -17.7kW/m^2 for higher altitudes. The heat flux characteristics and mean value remain constant above an altitude of 60 km.

Table 4.1.: Mean heat flux values for the simulated trajectory points during the ascent phase.

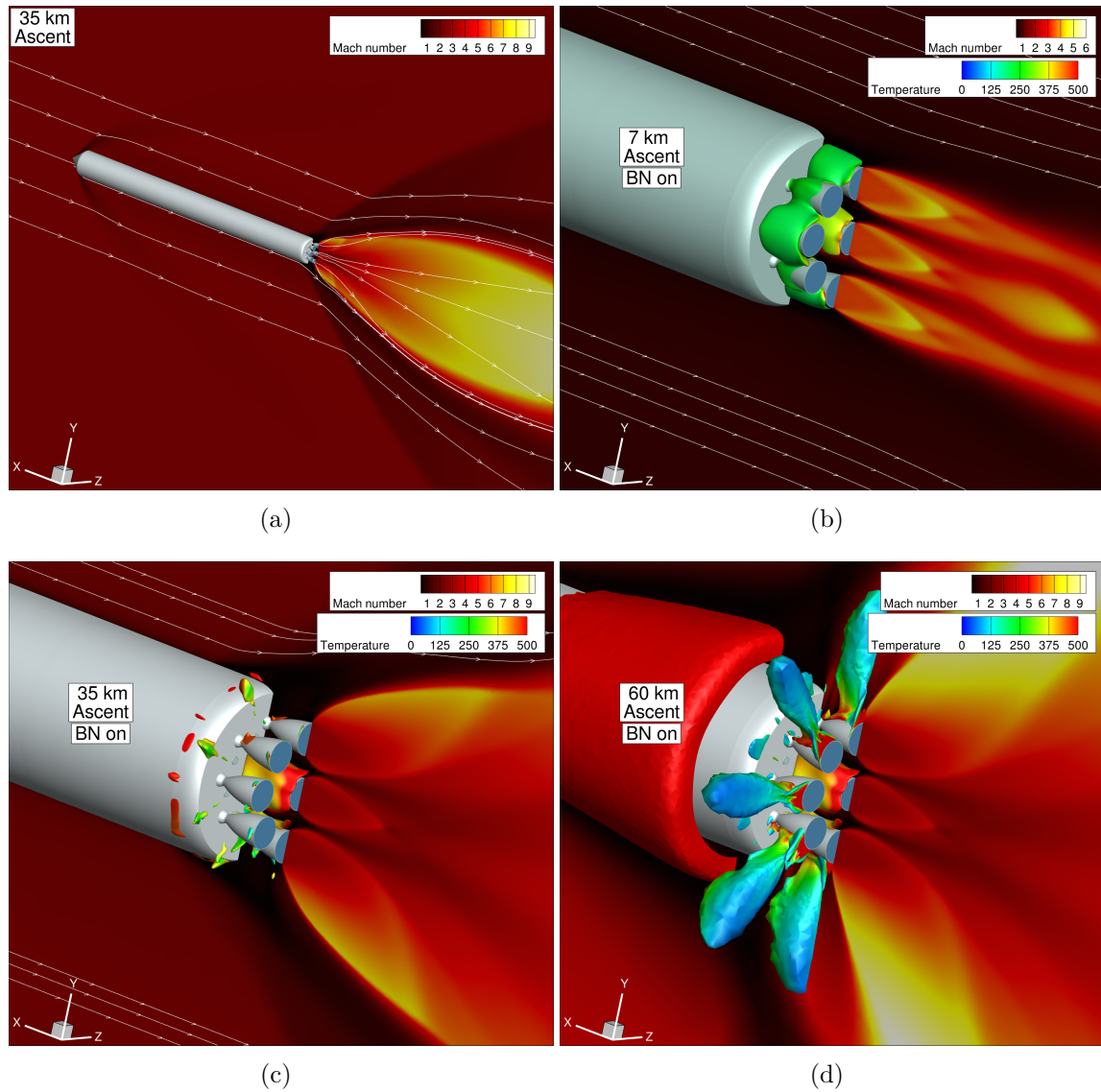| Trajectory point	height [km]	heat flux in [kW/m^2]
Ascent 1	7	-37.1
Ascent 2	35	-18.9
Ascent 3	60	-17.6
Ascent 4	86	-17.7

Figure 4.10.: Flowfield visualizations for the ascent trajectory a) full vehicle and plume structure at an altitude of 35 km. b) Aft-bay region and iso-surface of negative axial velocity of $u < -25$ m/s for an altitude of 7 km. c) Aft-bay region and iso-surface of negative axial velocity of $u < -200$ m/s for an altitude of 35 km. d) Aft-bay region and iso-surface of negative axial velocity of $u < -200$ m/s for an altitude of 60 km.

Note: The temperature colorscale for the iso-surface differs from the one in fig. 4.2.

Figure 4.11.: Comparison of the heat flux distribution along the baseplate for altitudes of 7 km and 35 km during the ascent phase with all main engines and bleed nozzles being active.

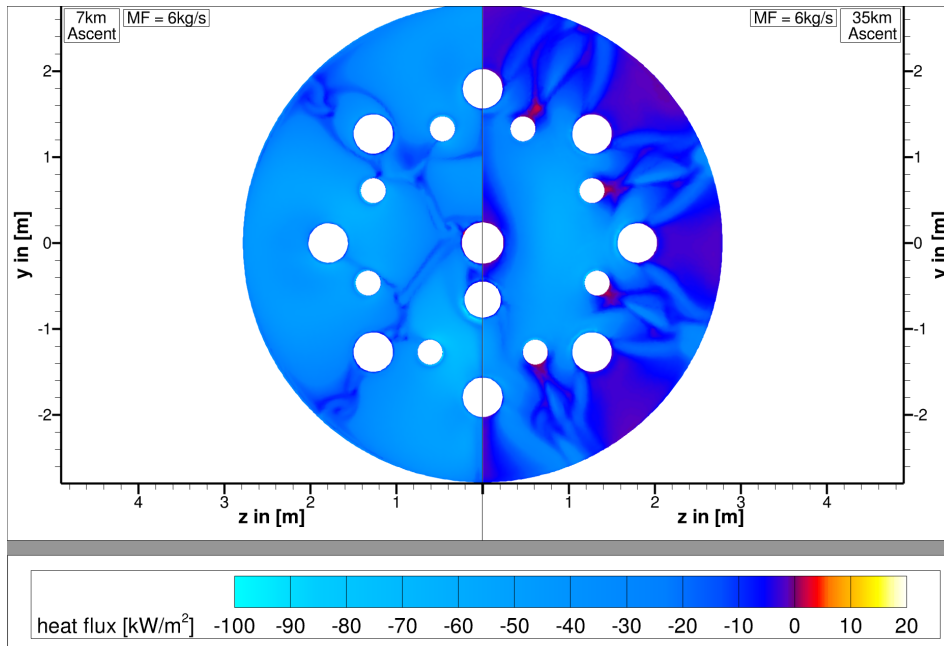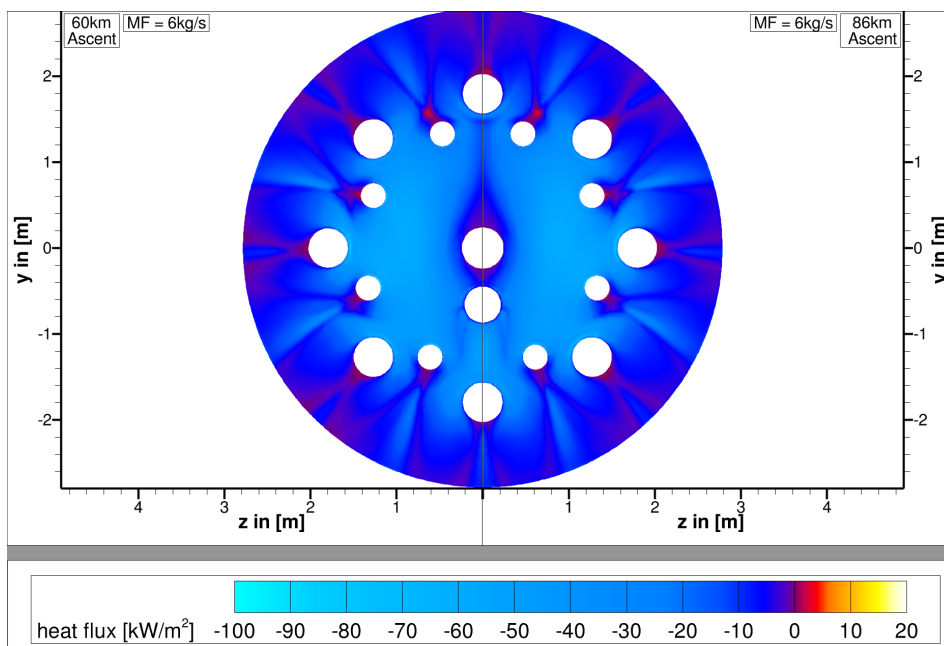

Figure 4.12.: Comparison of the heat flux distribution along the baseplate for altitudes of 60 km and 86 km during the ascent phase with all main engines and bleed nozzles being active.

4.5. Flowfield and thermal loads during the descent trajectory

This section is devoted to the discussion of the flowfield results and heat flux characteristics during the retro-burn phase. The altitudes of the two simulated trajectory points are 60 km and 40 km, with the corresponding free stream conditions in tab.(3.1). The heat flux distribution along the baseplate is plotted in fig.(4.13). A visualization of the flowfield at the representative trajectory points is given in fig.(4.14). The Mach number is plotted in grey-scale, while the 3D streamline-color indicates the temperature. To give a direct comparison of the flowfield structure for the two distinct trajectory points, the same area of the computational domain is visualized for the corresponding field cuts in the plane of activated and deactivated bleed nozzles indicated in fig.(4.13).

(a)   (b)

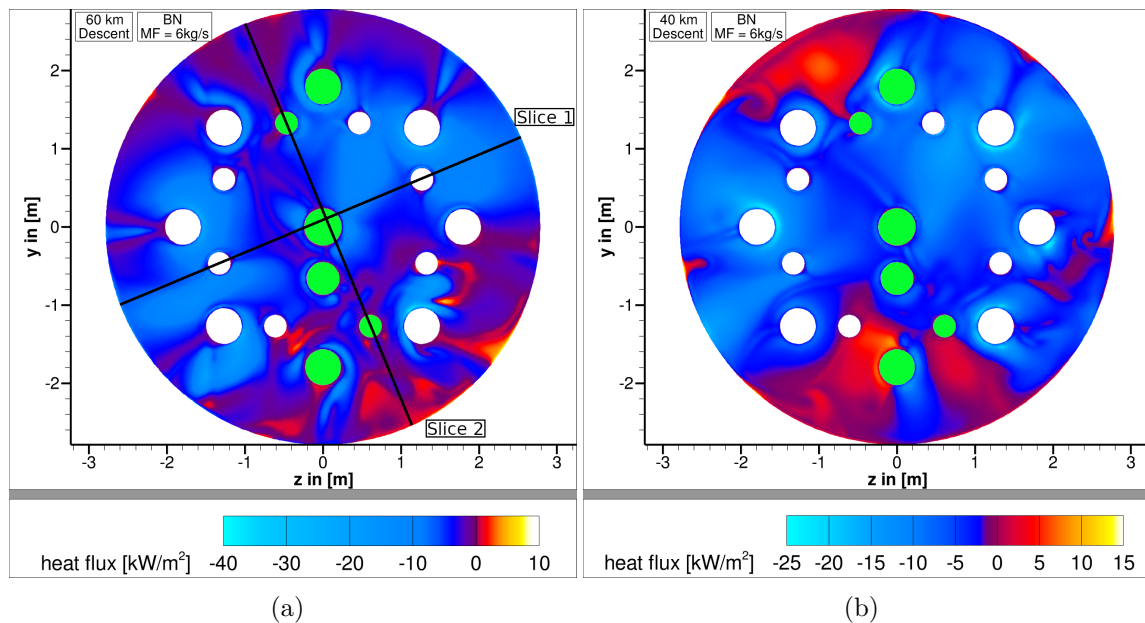Figure 4.13.: Heat flux distribution along the baseplate for an altitude of (a) 60 km and (b) 40 km during the descent and retro-burn phase. The indication of the field cuts for the flow field visualization are given by the black lines and name tags in the plot for an altitude of 60 km. Additionally the active main engines and bleed nozzles are marked by a green coloration of the baseplate openings.

In general the same flowfield characteristics which were already discussed in sec. 4.2 can be observed for the two configurations during the descent phase. However, due to the smaller atmospheric pressure for the 60 km case, the underexpansion ratio of the nozzles increases, leading to a larger spatial extent of the supersonic exhaust jets. Consequently, the stand-off distance and size of the of the Mach disk and barrel shock decrease during the retro-burn phase.

For an altitude of 60 km, strong recirculation regions of the hot main engine exhaust, indicated by the temperature colored streamlines, can be identified around the lower third of the RET-1S first stage. Due to the significantly larger exhaust plumes and recirculation regions for higher altitudes, the shielding effect of the main engines on the vehicle baseplate against the incoming free stream increases. The aft-bay is fully enveloped in the exhaust plume in the plane of deactivated bleed nozzles (Slice 1), preventing the entrainment of the main engine exhaust and a shift of the recirculation region further upstream along the vehicle can be observed, compared to the flowfield for an altitude of 40 km. Additionally a weak influence of the main engine exhaust jets in the peripheral aft-bay region can be identified in the plane with deactivated bleed nozzles. This leads to the same heat flux characteristics behind the baseplate openings of the outer main engines, which were observed for the same altitude during the ascent phase (compare to fig.(4.12)). The flow in the central baseplate region is dominated by the cold bleed nozzle outflow. The base flow characteristics are comparable to the results discussed in sec.(4.2). However, for

Table 4.2.: Mean heat flux values for the simulated trajectory points during the descent phase.

Trajectory point	height [km]	heat flux in [kW/m^2]
Decent 1	60	-4.4
Decent 2	40	-2.8

an altitude of 60 km the constriction of the main engine exhaust is weaker and the secondary exhaust jets themselves are highly underexpanded. Therefore a smaller amount of the main engine exhaust is entrained around the backwards facing step of the aft-bay and the intensity of the heat flux hot spots decreases. This behaviour can be seen by comparing the same closeup-flowfield in close proximity to the bleed nozzle outflow for the two altitudes. The recirculation region for the lower altitude of 40 km is larger, more distinct and extends deeper into the main engine cavities

(fig.(4.14 (d))). The heat flux values are in range of [-40;9] kW/m^2 for an altitude of 60 km and in range of [-25; 15] kW/m^2 for an altitude of 40 km. The overall heat flux and mean values in tab.(4.2) indicate that the thermal loads for the higher altitude of 60 km are slightly smaller compared to the the altitude of 40 km.
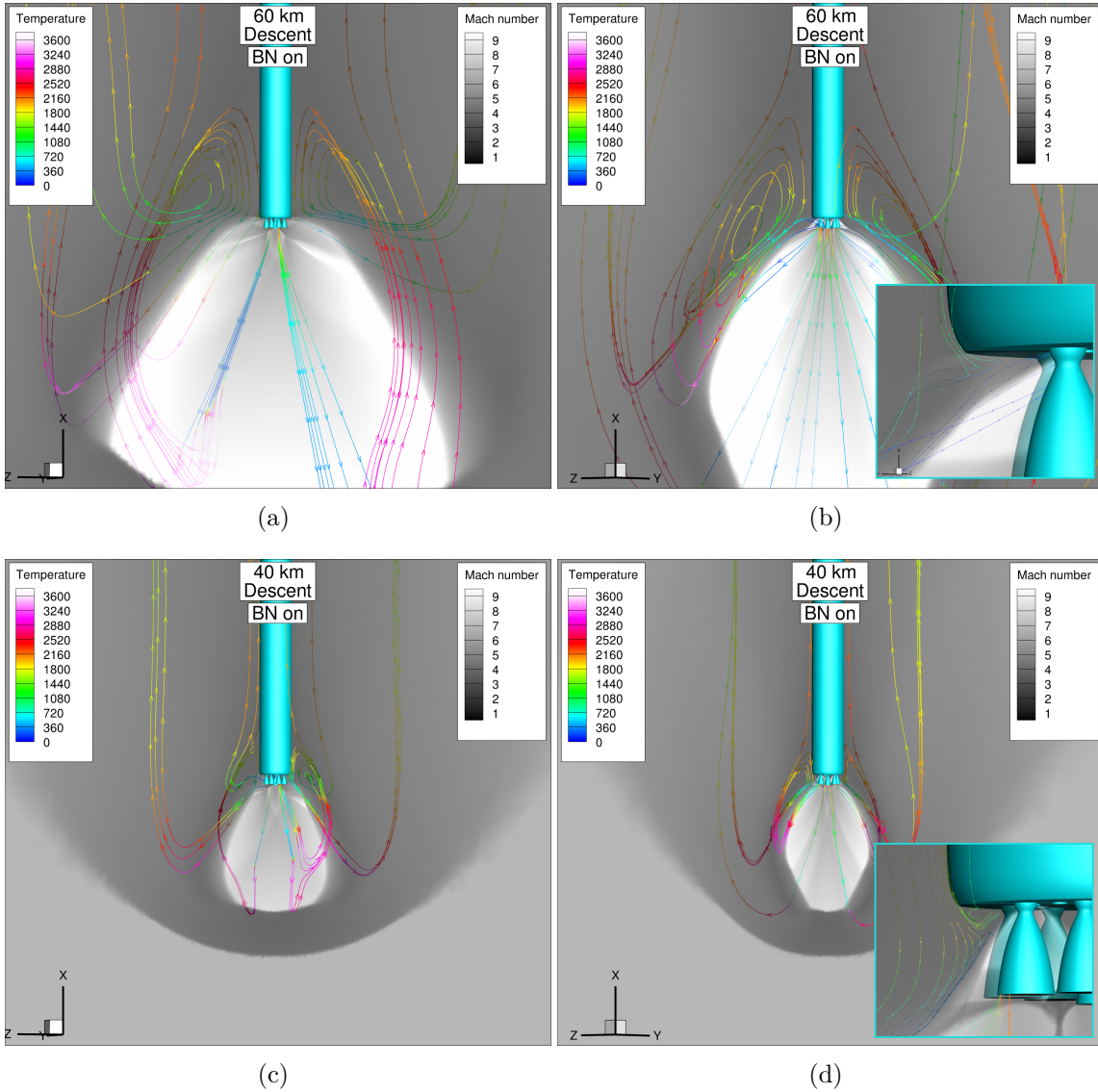
Figure 4.14.: Flowfield visualization of the descent phase for an altitude of 40 km and 60 km. The Mach number distribution is plotted for the corresponding Slice in gray-scale and the 3D streamlines are colored with the temperature color map. (a) Slice 1 through the plane of deactivated bleed nozzles for an altitude of 40 km perpendicular to (b) Slice 2 with active bleed nozzles for an altitude of 40 km. Slice indication is given in fig.(4.4). (c) Slice 1 through the plane of deactivated bleed nozzles for an altitude of 60 km perpendicular to (d) Slice 2 with active bleed nozzles for an altitude of 60 km. A closeup of the streamlines in the aft-bay region is provided.

5. Conclusion and outlook

In this work, the influence of additional fuel outflow from secondary nozzles in bleed engine and gas generator cycles on the base heating of a reusable launch vehicle were investigated by conducting 3D CFD simulations of the flowfield. All simulations were done using a steady-state RANS approach together with a one-equation Spalart-Allmaras turbulence model and a reduced 19-step Jachimowski mechanism for the chemistry modelling. The isothermal wall temperature was set to 600 K in all cases.

A short description concerning the funtionality of the two observed engine cycles was given and the governing equations for calculating the chamber conditions of the secondary nozzles from existing engine configurations were derived. In order to introduce the observed flow field characteristics and to provide a better understanding of the numerical results, the outflow from singular nozzles and the plume-plume interactions in clustered main engine arrays for the ascent and retro-propulsion phase of an RLV were described. A detailed description of the numerical setup, including the boundary conditions along the flight trajectory, the numerical mesh and bleed nozzle arrangement and the derivation of the secondary nozzle exhaust flow was provided. Additonally a grid convergence study was conducted to provide an assessment of the numerical uncertainties and to confirm the validity of the results. The calculated GCI values and small numerical errors indicate a sufficient resolution of the numerical mesh and a converged solution.

The influence of the additonal fuel outflow from the secondary nozzles was identified for the bleed engine cycle by comparing numerical results for activated and deactivated secondary nozzles. The simulations were done for an altitude of 35 km along the ascent trajectory and for an altitude of 40 km during the retro-burn phase. Although the additional exhaust gas from the secondary nozzles only makes up about 2% of the main engine exhaust, the high outflow and jet velocity prevent the recirculation of the hot main engine exhaust and the creation of updraft plumes.

5. Conclusion and outlook

Therefore a significant reduction of the thermal loads was observed. The mean heat flux was reduced from $\bar{q}_{\text{BN off, ASC}} = 48.2 \text{ kW/m}^2$ to $\bar{q}_{\text{BN on, ASC}} = -18.9 \text{ kW/m}^2$ for the ascent case and from $\bar{q}_{\text{BN off, DEC}} = 20.9 \text{ kW/m}^2$ to $\bar{q}_{\text{BN on, DEC}} = -2.8 \text{ kW/m}^2$ for the descent case. Since the isothermal wall temperature of the vehicle is set to 600 K in all simulations, the negative heat flux values do not indicate a cooling of the baseplate. Instead, these values point out an overall reduction of the thermal loads.

The RET-1S vehicle is based on the RETALT1 first stage. Therefore, the generated results in case of deactivated secondary nozzles are comparable to the aerothermal database of the RETALT1-vehicle [23]. Even though the local heat flux values in the central region around the baseplate perturbations of the secondary nozzles are increased, the same flow field and heat flux characteristics were observed.

Due to the ejection of the pure hydrogen gas in bleed engine cycles near the high temperature main engine exhaust, it was proposed, that post combustion might occur. The post-combustion of the unburned hydrogen could have lead to significantly increased thermal loads on the baseplate of the vehicle and changed requirements on the TPS. However, due to the small exhaust gas temperatures below the combustion conditions of hydrogen and the small amount of ambient oxygen present in the aft-bay, no post-combustion was observed. Additionally, it was supposed, that the changed exhaust gas mixture in the gas generator cycle and the higher total temperature of the jet might lead to conditions were post-combustion was possible, however this was not the case either. Therefore, due to the similar outflow temperatures of the secondary nozzles in the two engine cycles, the overall same flowfield and heat flux characteristics were observed.

The thermal loads for representative points along the flight trajectory were characterized. During the ascent phase, different flow regimes and exhaust plume characteristics are observed due to the decreasing ambient pressure and increasing flight Mach number. For small altitudes below 7 km only slightly underexpanded exhaust jets with weak plume-plume interactions are observed. With an increasing underexpansion ratio, the spatial extend of the exhaust jets and plume-plume interactions increase. The exhaust plume surrounds the baseplate and aft-bay region, leading to a footprint of the main engine exhaust jets in the peripheral region of the baseplate. With increasing altitude, the heat flux on the baseplate remains constant.

For the retro-burn maneuver 3 of the main engines and the corresponding secondary nozzles are in operation. The highly underexpanded main engine exhaust jets have

a shielding effect on the baseplate and aft-bay region of the vehicle. This effect decreases with decreasing altitude due to the smaller spatial extend of the exhaust jets. While the bleed nozzle outflow leads to reduced heat flux values in the central region of the baseplate, a constriction of the main engine jets in the plane of active secondary nozzles occurs. This leads to the entrainment of the hot main engine exhaust and local hot spots in the heat flux distribution in the plane of active secondary nozzles. The overall thermal loads are significantly smaller compared to configurations without the additional outflow.

To sum up, the additional cold gas outflow from secondary nozzles in bleed engine and gas generator cycles lead to a significant change of the flowflield and heat flux characteristics in the aft-bay region of the observed launch vehicle. Since the flight conditions are the same for an RLV and conventional space transport system, the outflow of these secondary nozzles has to be considered and simulated for launch vehicles in general. The generated results for the observed case raise the the question, if closed stage combustion cycles, which are mainly preferred due to their efficient usage of the oxidizer and fuel, are the optimal choice for RLVs. The reduced thermal loads on the vehicle baseplate owing to the secondary exhaust jets in open engine cycles could allow a reduction of the TPS thickness and mass. This might also lead to lower refurbishment costs and times of RLVs in between launches.

In this work a launch vehicle with 9 main engines was observed and a positive influence of the bleed nozzle exhaust was identified on the base heat flux. The recent system failure of the SpaceX Starship vehicle raises the concern, that this could not be the case for launch vehicles applying up to 33 main engines. During the Starship launch and ascent phase, a scorching wihte-red coloration of the baseplate was observed, indicating significant thermal loads on the baseplate. Therefore one focus of subsequent studies should be the identification of the thermal loads for engine clusters applying a larger amount of main engines. Additionally, trajectory points below an altitude of 7 km should be simulated to identify the influence of the secondary exhaust jets. Due to the denser atmosphere and the entrainment of oxygen in the aft-bay region for confined jet structures post-combustion of the fuel rich exhaust gas could be observed.

Another vital point is the ground interaction during the launch sequence of the vehicle. While single supersonic jet impingement system have been studied before by e.g. Feldner [14], Ertl [13] and Gao [40], no research has been published concerning

the ground interaction of clustered main engine exhaust jets. The high generation of thrust might lead to critical mechanical and thermal loads on the baseplate, especially for flat start-platforms without flow deflectors, and might cause severe damage of the launch site.

Finally the mechanical loads of the secondary nozzles on the main engine walls need to be characterized in order to avoid potential problems during the gimbaling process of the main engines.

A. RETALT1 vehicle characteristics and geometric values

Stage Characteristics	1st Stage	2nd Stage	Fairing	Total
Number of Engines	9	1.0	-	10.0
Reusability	+	+/-	-	+/-
Height [m]	71.2	19.8	12.0	103.0
Diameter [m]	6.00	6.00		6.00
Mass full (GLOW) [t] (incl. Payload)	680.8	204.2	2.5	899.0
Stage Rate	75.7%	24.3%		
Structure Coefficient	8.7%	8.3%		
Mass structure [t]	59.3	16.7		75.9
Propellant mass (incl. descent porpellant) [t]	621.5	187.5		809.0
Descent propellant [t]	50.0	0		50.0
Propellant reserve and residuals mass [t]	7.500	2.500		10.0
Engines	RETALT1-LHLOX-E15-FS	RETALT1-LHLOX-E70-FS		
Engine Cycle	Gasgenerator	Gasgenerator		
Oxidator/Propellant	LOX/LH2	LOX/LH2		
Expansion Ratio	15	70		
Specific Impuls SL [s]	372.2	294.4		
Specific Impuls Vac [s]	401.6	431.9		
Thrust SL [kN]	9x1179 = 10614	1x930 = 930		
Thrust Vac [kN]	9x1273 = 11453	1x1364 = 1364		

Figure A.1.: RETALT1 vehicle characteristics and geometric values taken from Marwege et al.[25].

B. Parameters of the cylindrical and conical grid refinement regions

Table B.1.: Parameters of the cylindrical and conical grid refinement regions for the 3 different meshes used in the grid convergence study.

Parameters	cylindrical GF region	conical GF region
x_1-coordinate in [mm]	-910	1750.6884
x_2-coordinate in [mm]	1750.6884	65000
radius 1 in [mm]	3400	3400
radius 2 in [mm]	3400	50000
fine mesh		
cell size 1 in [mm]	22.2	9.626
cell size 2 in [mm]	22.2	740.740
medium mesh		
cell size 1 in [mm]	30	13
cell size 2 in [mm]	30	1000
coarse mesh		
cell size 1 in [mm]	40.5	17.5
cell size 2 in [mm]	40.5	1350

C. Side view on the flowfield characteristics during descent for an altitude of 40 km
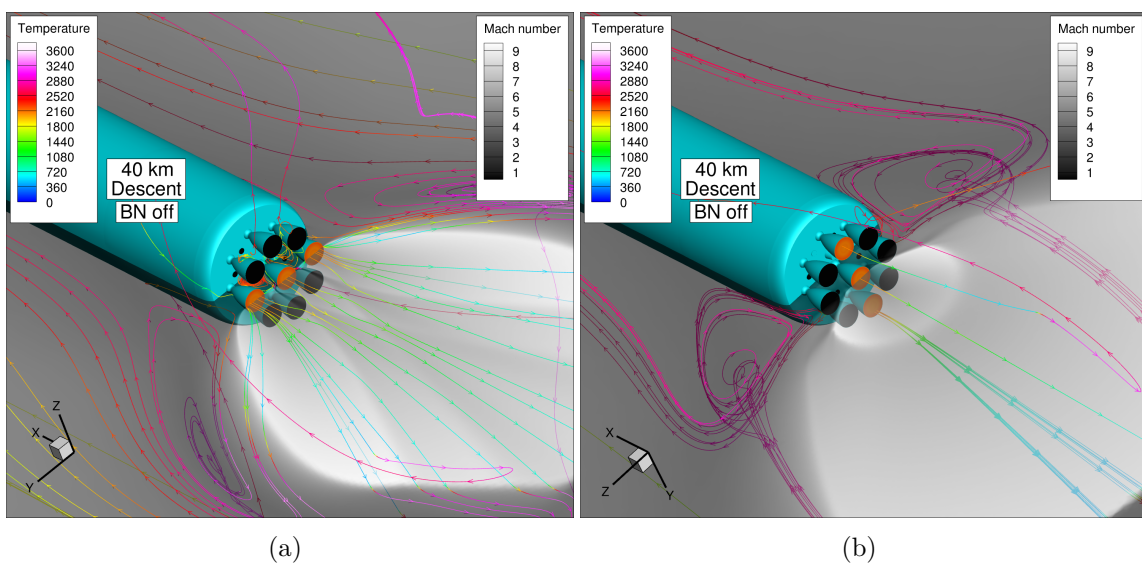

Figure C.1.: Side view of the flowfield visualization for the simulated case with deactivated bleed nozzles. The Mach number distribution is plotted for the corresponding Slice in gray-scale and the streamlines are colored with the temperature color map. Active main engines are indicated by the orange outflow marker, representing the temperature of the hot main engine exhaust. (a) Slice 1 through the active main engines and x-z-plane at the position y=0. (b) Slice 2 perpendicular to Slice 1 along the x-y-plane with z=0.

Bibliography

[1] John Anderson. *EBOOK: Fundamentals of Aerodynamics (SI units)*. McGraw hill, 2011.

[2] J. Boussinesq. Essai sur la théorie des eaux courantes. *Mem. Présenté Acad. Sci.*, 23:S. 46, 1877.

[3] P. Brossel, S. Eury, P. Signol, H. Laporte-Weywada, and J.B. Micewics. Development status of the vulcain engine. *31st Joint Propulsion Conference and Exhibit*, 1995.

[4] Steffen Callsen. Critical analysis of rocket lab neutron launcher and missions. Technical report, März 2022. URL `https://elib.dlr.de/185517/`.

[5] I. B. Celik, U. Ghia, P. J. Roach, C. J. Freitas, H. Coleman, and P. E. Raad. Procedure for estimation and reporting of uncertainty due to discretization in cdf application. *Journal of Fluids Engineering - Transactions of the ASME*, 130(7), July 2008.

[6] Lance A. Davis. First stage recovery. *Engineering*, 2(2):152–153, 2016. ISSN 2095-8099. doi: https://doi.org/10.1016/J.ENG.2016.02.007. URL `https://www.sciencedirect.com/science/article/pii/S2095809916309407`.

[7] Alessandro de Iaco Veris and Alessandro de Iaco Veris. *Fundamental Concepts on Liquid-Propellant Rocket Engines*. Springer, 2021.

[8] G. De Zaiacomo, R. Blanco Arnao, G. amd Bunt, and D. Bonetti. Mission engineering for the retalt vtvl launcher. In *CEAS Space J 14, 533–549*, 2022. URL `https://doi.org/10.1007/s12567-021-00415-y`.

[9] Houshang B Ebrahimi, Jay Levine, and Alan Kawasaki. Numerical investigation of twin-nozzle rocket plume phenomenology. *Journal of Propulsion and Power*, 16(2):178–186, 2000.

Bibliography

[10] Tobias Ecker, Franziska Zilker, Etienne Dumont, Sebastian Karl, and Klaus Hannemann. Aerothermal analysis of reusable launcher systems during retro-propulsion reentry and landing. 05 2018.

[11] Tobias Ecker, Sebastian Karl, Etienne Dumont, Sven Stappert, and Daniel Krause. Numerical study on the thermal loads during a supersonic rocket retropropulsion maneuver. *Journal of Spacecraft and Rockets*, 57(1):131–146, 2020.

[12] Ahmed F El-Sayed. *Fundamentals of aircraft and rocket propulsion.* Springer, 2016.

[13] Moritz Ertl, Yannik Feldner, and Tobias Ecker. Numerical investigation of ground heat fluxes from supersonic jet impingement during vertical landing of a reusable first stage demonstrator. In *2nd International Conference on High-Speed Vehicle Science & Technology HISST 2022*, number 0035, pages 1–13. CEAS, September 2022. URL `https://elib.dlr.de/187883/`.

[14] Yannik Feldner. Numerische Untersuchung des Wärmeübergangs bei Strahl-Wand-Wechselwirkungen unterexpandierter überschallprallstrahlen mit einer glatten Oberfläche, December 2020. URL `https://elib.dlr.de/143454/`.

[15] Yannik Feldner, Moritz Ertl, Tobias Ecker, and Sebastian Karl. Numerical investigation of the effects of post-combustion due to fuel outflow in bleed engine cycles of a retro propulsion-assisted launch vehicle. In EUCASS and CEAS, editors, *10th EUCASS - 9th CEAS 2023*, Juli 2023. URL `https://elib.dlr.de/193848/`.

[16] Erwin Franquet, Vincent Perrier, Stéphane Gibout, and Pascal Bruel. Review on the underexpanded jets. 09 2015. doi: 10.13140/RG.2.1.2640.6883.

[17] Uwe Ganzer. *Gasdynamik.* Springer-Verlag, 2013.

[18] Peter Gerlinger, Helge Möbus, and Dieter Brüggemann. An implicit multigrid method for turbulent combustion. *Journal of Computational Physics*, 167(2): 247–276, 2001.

[19] Klaus Hannemann, Jan M Schramm, Alexander Wagner, Sebastian Karl, and Volker Hannemann. A closely coupled experimental and numerical approach

for hypersonic and high enthalpy flow investigations utilising the HEG shock tunnel and the DLR TAU code. Technical report, German Aerospace Center Braunschweig (Germany), Institute of Aerodynamics and Flow Technology, 2010.

[20] Volker Hannemann. Numerical simulation of shock-shock interactions considering chemical and thermal nonequilibrium. *Cologne, Germany: Deutsche Forschungsanstalt fuer Luft- und Raumfahrt(DLR-Forschungsbericht 97-07), 1997.*, 1997.

[21] K. V. Klinkov. *Unsteady gas flows and particle dynamics in the shock layer formed by the impingement of a supersonic two-phase jet onto a plate.* DLR, Bibliotheks-und Informationswesen, 2005.

[22] D.E. Koelle and H. Kuczera. Sänger ii, an advanced launcher system for europe. *Acta Astronautica*, 19(1):63–72, 1989. ISSN 0094-5765. doi: https://doi.org/10.1016/0094-5765(89)90009-X. URL `https://www.sciencedirect.com/science/article/pii/009457658990009X`.

[23] Mariasole Laureti and Sebastian Karl. Aerothermal databases and load predictions for retro propulsion-assisted launch vehicles (retalt). *CEAS Space Journal*, 14(3):501–515, 2022.

[24] Detlef Manski, Christoph Goertz, Hagen-D Saßnick, James R Hulka, B David Goracke, and Daniel JH Levack. Cycles for earth-to-orbit propulsion. *Journal of Propulsion and Power*, 14(5):588–604, 1998.

[25] Ansgar Marwege, Josef Klevanski, Johannes Riehmer, Daniel Kirchheck, Sebastian Karl, Davide Bonetti, J. Vos, Matthew Jevons, Anett Krammer, and João Carvalho. Retro propulsion assisted landing technologies (retalt): Current status and outlook of the eu funded project on reusable launch vehicles. In *Paper presented at the 70th International Astronautical Congress, 21-25 October 2019, Washington D.C., United States*, October 2019. URL `https://elib.dlr.de/132566/`. Paper presented at the 70th International Astronautical Congress, 21-25 October 2019, Washington D.C., United States www.iafastro.org.

[26] Ansgar Marwege, Ali Gülhan, Josef Klevanski, Christian Hantz, Sebastian Karl, Mariasole Laureti, Gabriele De Zaiacomo, Jan Vos, Matthew Jevons, Christoph

Thies, et al. Retalt: review of technologies and overview of design changes. *CEAS Space Journal*, 14(3):433–445, 2022.

[27] B. McBride and S. Gordon. *NASA-Glenn Chemical Equilibrium Program CEA2*. https://cearun.grc.nasa.gov/, 2004, Abfrage: 11.10.2020.

[28] Manish Mehta, Aaron T Dufrene, Mark Seaford, and Kyle Knox. Space launch system base heating test: Environments and base flow physics. In *54th AIAA Aerospace Sciences Meeting*, page 0547, 2016.

[29] Normal T Musial and James J Ward. *Base flow characteristics for several four-clustered rocket configurations at mach numbers from 2.0 to 3.5*. National Aeronautics and Space Administration, 1961.

[30] R Nallasamy, M Kandula, L Duncil, and P Schallhorn. Base flow and heat transfer characteristics of a four-nozzle clustered rocket engine: Effect of nozzle pressure ratio. In *48th AIAA Aerospace Sciences Meeting*, number KSC-2009-281, 2010.

[31] Antoine Patureau de Mirand, Jean-Marc Bahu, and Olivier Gogdet. Ariane next, a vision for the next generation of ariane launchers. *Acta Astronautica*, 170:735–749, 2020. ISSN 0094-5765. doi: https://doi.org/10.1016/j.actaastro. 2020.02.003. URL https://www.sciencedirect.com/science/article/pii/ S0094576520300631.

[32] Daniel Rasky, R Bruce Pittman, and Mark Newfield. The reusable launch vehicle challenge. In *Space 2006*, page 7208. 2006.

[33] L. F. Richardson. Ix. the approximate arithmetical solution by finite differences of physical problems involving differential equations, with an application to the stresses in a masonry dam. *Philosophical Transactions of the Royal Society of London. Series A, Containing Papers of a Mathematical or Physical Character*, 210(459-470):307–357, 1911.

[34] D. Schwamborn, T. Gerhold, and R. Heinrich. The dlr tau-code: recent applications in research and industry. 2006.

[35] Martin Sippel, Armin Herbertz, Holger Burkhardt, Takayuki Imoto, Dietrich Haeseler, and Andreas Götz. Studies on expander bleed cycle engines for launch-

ers. In *39th AIAA/ASME/SAE/ASEE Joint Propulsion Conference and Exhibit*, page 4597, 2003.

[36] CENTAUR Software. *Centaur Version 14*. https://www.centaursoft.com/, Abfrage: 19.10.2020.

[37] Philippe Spalart and Steven Allmaras. A one-equation turbulence model for aerodynamic flows. *AIAA*, 439, 01 1992. doi: 10.2514/6.1992-439.

[38] Dassault Systems. *Catia v5*. https://www.3ds.com/de/produkte-und-services/catia/, Abfrage: 19.10.2020.

[39] Ben Thornber, A. Mosedale, Dimitris Drikakis, David Youngs, and R.J.R. Williams. An improved reconstruction method for compressible flows with low mach number features. *Journal of Computational Physics*, 227:4873–4894, 05 2008. doi: 10.1016/j.jcp.2008.01.036.

[40] Yuyan Tian, Wenhao Li, Pu Xue, and Zhenxun Gao. Numerical studies on heat transfer of supersonic combustion-gas jet impingement on perpendicular flat plate. *Heat Transfer Engineering*, 43(8-10):864–878, 2022. doi: 10.1080/01457632.2021.1906518. URL https://doi.org/10.1080/01457632.2021.1906518.

[41] Finn van Donkelaar and James Penna. Preliminary experimental investigations of an electrothermal hypervelocity accelerator. 01 2019. doi: 10.2514/6.2019-2006.

[42] Yasuhiro Wada and Meng Liou. A flux splitting scheme with high-resolution and robustness for discontinuities. *32nd Aerospace Sciences Meeting and Exhibit*, 07 1994. doi: 10.2514/6.1994-83.

[43] D. C. Wilcox. *Turbulence Modelling in CFD, 3. Auflage*. DCW Industries Inc., 2006.

[44] Franziska Zilker. Aerothermal analysis of re-usable first stage during rocket retro-propulsion. Master's thesis, Januar 2018. URL https://elib.dlr.de/119265/.

Acknowledgements

Erklärung Ich versichere hiermit, dass ich die vorliegende Arbeit ohne fremde Hilfe selbstständig verfasst und nur die von mir angegebenen Quellen und Hilfsmittel verwendet habe. Wörtlich oder sinngemäß aus anderen Werken entnommene Stellen habe ich unter Angabe der Quellen kenntlich gemacht. Die Richtlinien zur Sicherung der guten wissenschaftlichen Praxis an der Universität Göttingen wurden von mir beachtet. Eine gegebenenfalls eingereichte digitale Version stimmt mit der schriftlichen Fassung überein. Mir ist bewusst, dass bei Verstoß gegen diese Grundsätze die Prüfung mit nicht bestanden bewertet wird.

Göttingen, den September 7, 2023

(Yannik Feldner)